Complex Organic Molecules toward Embedded Low-mass Protostars

Draft version May 16, 2017
Preprint typeset using LaTeX style AASTeX6 v. 1.0

COMPLEX ORGANIC MOLECULES TOWARDS EMBEDDED LOW-MASS PROTOSTARS

Jennifer B. Bergner[1], Karin I. Öberg[2], Robin T. Garrod[3], Dawn M. Graninger[2]

[1]Harvard University Department of Chemistry and Chemical Biology, Cambridge, MA 02138, USA
[2]Harvard-Smithsonian Center for Astrophysics, Cambridge, MA 02138, USA
[3]University of Virginia Departments of Chemistry and Astronomy, Charlottesville, VA 22904, USA

ABSTRACT

Complex organic molecules (COMs) have been observed towards several low-mass young stellar objects (LYSOs). Small and heterogeneous samples have so far precluded conclusions on typical COM abundances, as well as the origin(s) of abundance variations between sources. We present observations towards 16 deeply embedded (Class 0/I) low-mass protostars using the IRAM 30m telescope. We detect CH_2CO, CH_3CHO, CH_3OCH_3, CH_3OCHO, CH_3CN, HNCO, and HC_3N towards 67%, 37%, 13%, 13%, 44%, 81%, and 75% of sources respectively. Median column densities derived using survival analysis range between 6.0x10^{10} cm^{-2} (CH_3CN) and 2.4x10^{12} cm^{-2} (CH_3OCH_3) and median abundances range between 0.48% (CH_3CN) and 16% (HNCO) with respect to CH_3OH. Column densities for each molecule vary by about one order of magnitude across the sample. Abundances with respect to CH_3OH are more narrowly distributed, especially for oxygen-bearing species. We compare observed median abundances with a chemical model for low-mass protostars and find fair agreement, although some modeling work remains to bring abundances higher with respect to CH_3OH. Median abundances with respect to CH_3OH in LYSOs are also found to be generally comparable to observed abundances in hot cores, hot corinos, and massive young stellar objects. Compared with comets, our sample is comparable for all molecules except HC_3N and CH_2CO, which likely become depleted at later evolutionary stages.

1. INTRODUCTION

Complex organic molecules (COMs), hydrogen-rich molecules with 6 or more atoms, have been observed towards high- and low-mass star forming regions, molecular outflows, and prestellar cores (e.g. Blake et al. 1987; Fayolle et al. 2015; Bottinelli et al. 2004b, 2007; Arce et al. 2008; Öberg et al. 2010; Bacmann et al. 2012; Cernicharo et al. 2012). COMs formed at these early stages of star formation can become incorporated into protoplanetary disks (Visser et al. 2009, 2011) and further into planetesimals and planets, seeding nascent planets with complex organic material. COM abundances around protostars are thus of considerable interest for the study of origins of life. Low-mass stars host most planetary systems, and so the molecular inventories towards low-mass young stellar objects (LYSOs) are most relevant for characterizing potentially habitable environments. Indeed, our own sun is a low-mass star, and observations of COMs towards LYSOs can inform our understanding of the protostellar phase of our own solar system, as well as the uniqueness of our solar system relative to others like it.

COMs are thought to mainly form within the ice mantles coating interstellar dust grains (Herbst & van Dishoeck 2009). First, hydrogenation of atoms or small molecules forms small saturated COMs such as CH_3OH, so-called "zeroth-generation" species. Photolysis or radiolysis can then dissociate small molecules to form radicals (reviewed in Öberg 2016). During protostellar collapse the cloud material is heated, enabling diffusion and recombination of these small molecules and radicals to form larger complex molecules referred to as "first-generation" species. Modeling has shown that this becomes efficient above 30K (Garrod & Herbst 2006). This mechanism produces the same types of molecules that are commonly observed in YSOs, although some COMs are still underproduced in models compared to observations (Caselli & Ceccarelli 2012). Once temperatures reach 100-300K, large molecules desorb and react in the gas phase to form "second-generation" molecules. Gas-phase reactions may also play a role in first-generation chemistry via the desorption of small molecules, namely CH_3OH, followed by reaction in the gas phase rather

Based on observations carried out under project numbers 003-14 and 006-13 with the IRAM 30m Telescope. IRAM is supported by INSU/CNRS (France), MPG (Germany) and IGN (Spain)

than on grain-surfaces (e.g. Balucani et al. 2015).

Both the ice and gas-phase chemistry scenarios predict a close connection between COMs and the original ice composition. Ice composition is known to vary between sources, especially CH_3OH ice abundances (Öberg et al. 2011a). Furthermore, the chemistry may depend on the stellar radiation field and the evolutionary stage of the source in question. Observed variations in chemical richness may then signify inherent variations between different sources, or simply that objects are observed at different evolutionary stages, or a combination of both. Which source of variability dominates will affect predictions on the chemical environment in which planets form during later stages of star formation, and how much this can vary between different sources.

LYSOs are thought to undergo evolution from prestellar cores to protostellar envelopes, which are termed hot corinos once the center is warm enough to sublimate water ice (e.g. Caselli & Ceccarelli 2012). COMs have been previously detected towards both envelopes and hot corinos of LYSOs (e.g. Cazaux et al. 2003; Bottinelli et al. 2004a, 2007; Öberg et al. 2011b). Öberg et al. (2014) combined these results from the literature with observations towards 6 young LYSOs and found that COM column densities and abundances span orders of magnitude between different sources. However, for several reasons it has been difficult to draw firm conclusions on typical abundances and the origin of variability between sources. These protostars span a range of evolutionary stages, from prestellar cores to evolved protostars with hot envelopes and no ice absorption. Moreover,the sample size is small (∼14 objects), and objects that were chosen for hosting interesting chemistry may not be representative of the true sample distribution.

Because of uncertainties in "typical" LYSO COM abundances, it is unclear how LYSOs compare with their massive counterparts (MYSOs) in terms of chemical richness. It has been claimed both that LYSOs are more enhanced in COMs than MYSOs (Bottinelli et al. 2007; Herbst & van Dishoeck 2009) and also that LYSO abundances are comparable or smaller than MYSO abundances (Bisschop et al. 2008; Öberg et al. 2011b). A better estimate of typical COM abundances around LYSOs is required to resolve whether these protostars indeed host distinct chemistries.

To clarify both the characteristic chemistry of LYSOs, as well as to make meaningful comparisons with MYSOs, a homogeneous and unbiased sample is required. Here we present an extension of the pilot survey in Öberg et al. (2014), yielding a total of 16 low-mass protostars. Both the 6 previously observed sources and the 10 new sources are Class 0/I protostars, enabling a direct comparison of the chemistry between sources at a similar evolutionary stage.

In Section 2 we describe the observations and data reduction. In Section 3 we present the results, first deriving column densities and rotational temperatures for the observed COMs. We derive median values for COM abundances from this sample using survival analysis in order to estimate characteristic abundance frequencies, as well as correlations between different COM species. In Section 4, we describe a warm-up model used to simulate chemistry around LYSOs, and present the model results. In Section 5 we comment on implications for formation chemistry based on our findings. We also compare our observational results with the chemical model, and with previous studies of different classes of objects.

2. OBSERVATIONS

Source selection and observation strategy are described in detail in Graninger et al. (2016). Briefly, 16 Class 0/I YSOs, identified by their IR spectral indices, were selected from the Spitzer *c2d* ice sample presented in Boogert et al. (2008) based on their location in the northern hemisphere and their ice abundances (Table 1). The sources were observed with the IRAM 30m telescope using the EMIR 90 GHz receiver and the Fourier Transform Spectrometer (FTS) backend. B1-a, B5 IRS1, L1489 IRS, IRAS 04108+2803, IRAS 03235+3004, and SVS 4-5 were observed June 12-16, 2013 at 93 - 101 GHz and 109 - 117 GHz. All other sources were observed on July 23-28, 2014 at 92 - 100 GHz and 108 - 116 GHz. All observations had a resolution of 200 kHz. The telescope beam size ranges from 27" at 92 GHz to 21" at 117 GHz. Excluding the highest frequency spectral window, the rms values range from 2-7 mK; for each source, the rms around the CH_3CN 6_0-5_0 transition at 110.383 GHz is listed in Table 1 to show the variability in rms between the sources observed.

Table 1. Source information of the complete 16-object c2d embedded protostar sample with ice detections

Source	R.A. (J2000.0)	Dec (J2000.0)	Cloud	L_{bol} $L_\odot$	M_{env} $M_\odot$	α^a_{IR}	N(CH_3OH) 10^{13} cm^{-2}	N($H_2O_{(ice)}$)^a 10^{18} cm^{-2}	$X^b_{CH_3OH(ice)}$ % H_2O	$X^b_{NH_3(ice)}$ % H_2O	rms (mK)
B1-a[c]	03:33:16.67	31:07:55.1	Perseus	1.3[d]	2.8[d]	1.87	10.21 [3.24]	10.39 [2.26]	<1.9	3.33 [0.98]	3.6
B1-c	03:33:17.89	31:09:31.0	Perseus	3.7[d]	17.7[d]	2.66	1.69 [0.51]	29.55 [5.65]	<7.1	<4.04	5.5

Table 1 continued

Table 1 *(continued)*

Source	R.A. (J2000.0)	Dec (J2000.0)	Cloud	L_{bol} $L_\odot$	M_{env} $M_\odot$	α^a_{IR}	$N(CH_3OH)$ 10^{13} cm^{-2}	$N(H_2O_{(ice)})^a$ 10^{18} cm^{-2}	$X^b_{CH_3OH(ice)}$ % H_2O	$X^b_{NH_3(ice)}$ % H_2O	rms (mK)
B5 IRS 1[c]	03:47:41.61	32:51:43.8	Perseus	4.7[d]	4.2[d]	0.78	1.77 [0.46]	2.26 [0.28]	<3.7	<2.09	7.0
HH 300	04:26:56.30	24:43:35.3	Taurus	1.27[e]	0.03[f]	0.79	0.24 [0.10]	2.59 [0.25]	<6.7	3.46 [0.90]	5.8
IRAS 03235+3004[c]	03:26:37.45	30:15:27.9	Perseus	1.9[d]	2.4[d]	1.44	1.17 [0.08]	14.48 [2.26]	4.2 [1.2]	4.71 [1.00]	4.2
IRAS 03245+3002	03:27:39.03	30:12:59.3	Perseus	7.0[d]	5.3[d]	2.70	1.54 [0.29]	39.31 [5.65]	<9.8	<4.40	3.7
IRAS 03254+3050	03:28:34.51	31:00:51.2	Perseus	–	0.3[d]	0.90	-	3.66 [0.47]	<4.6	6.66 [1.37]	3.9
IRAS 03271+3013	03:30:15.16	30:23:48.8	Perseus	0.8[d]	1.2[d]	2.06	0.42 [0.04]	7.69 [1.76]	<5.6	6.37 [1.86]	4.8
IRAS 04108+2803[c]	04:13:54.72	28:11:32.9	Taurus	0.62[e]	–	0.90	1.04 [0.44]	2.87 [0.4]	<3.5	4.29 [1.03]	4.0
IRAS 23238+7401	23:25:46.65	74:17:37.2	CB244	–	–	0.95	2.19 [1.01]	12.95 [2.26]	<3.6	<1.24	2.7
L1014 IRS	21:24:07.51	49:59:09.0	L1014	–	–	1.28	0.88 [0.56]	7.16 [0.91]	3.1 [0.8]	5.20 [1.43]	2.8
L1448 IRS1	03:25:09.44	30:46:21.7	Perseus	17.0[d]	16.3[d]	0.34	0.23 [0.04]	0.47 [0.16]	<14.9	<4.15	3.7
L1455 IRS3	03:28:00.41	30:08:01.2	Perseus	0.32[d]	0.2[g]	0.98	1.46 [0.88]	0.92 [0.37]	<12.5	6.21 [3.51]	3.9
L1455 SMM1	03:27:43.25	30:12:28.8	Perseus	3.1[d]	5.3[d]	2.41	1.48 [0.76]	18.21 [2.82]	<13.5	<8.29	4.1
L1489 IRS[c]	04:04:43.07	26:18:56.4	Taurus	3.7[e]	0.1[h]	1.10	0.69 [0.14]	4.26 [0.51]	4.9 [1.5]	5.42 [0.96]	5.4
SVS 4-5[c]	18:29:57.59	01:13:00.6	Serpens	38[i]	–	1.26	11.19 [4.29]	5.65 [1.13]	25.2 [3.5]	∼4.3	3.9

NOTE—Adapted from Graninger et al. (2016)
[a]Boogert et al. (2008), [b]Bottinelli et al. (2010), [c]Sources were observed by Öberg et al. (2014), [d]Hatchell et al. (2007), [e]Furlan et al. (2008),[f]Arce et al. (2008),[g]Enoch et al. (2009), [h]Brinch et al. (2007), [i]Pontoppidan et al. (2004)

Spectra were reduced using CLASS[1]. Global baselines were fit to each 4 GHz spectral window using several line-free windows. Each individual scan was baseline subtracted and averaged. The beam efficiency was modified using Ruze's equation with scaling factor 0.861 and sigma of 63.6 microns, resulting in beam efficiencies at the first, middle, and last channel of 0.8106, 0.7975, and 0.7830. Together with a forward efficiency of 0.95, the antenna temperature was converted to the main beam temperature T_{mb}. Literature source velocities were used to convert spectra to rest frequency, with fine-tuning adjustments made with the CH_3OH 2-1 and CN 1-0 ladders.

3. OBSERVATIONAL RESULTS

3.1. *Molecule Detections*

Figure 1 shows the spectra of all observed sources. A wide dispersion in line richness is evident in the sample. B1-a and SVS 4-5 are very line-dense, followed by a collection of moderately rich sources: B1-c, IRAS 23238, L1455 IRS3, B5 IRS1 L1455 SMM1, IRAS 03235, L1014 IRS, IRAS 04108, and IRAS 03235. Finally, L1489, HH 300, IRAS 03271, IRAS 03253, and L1448 IRS1 are quite line-poor. A selection of complex organic molecules that have been observed towards other high- or low-mass protostars are covered by our spectral setting. We have focused on COMs that were detected towards several of the sources in our survey: CH_3CHO, CH_3OCH_3, CH_3OCHO, and CH_3CN. For comparison, we also include the smaller organics HNCO and CH_2CO[2], as well as the carbon chain cyanide HC_3N. Line candidates within the observed frequency range were identified using the JPL[3] and CDMS[4] catalogs, limited by upper excitation energies less than 200 K.

CH_2CO, CH_3CHO, CH_3OCH_3, CH_3OCHO, CH_3CN, HNCO, and HC_3N are detected in 4, 6, 2, 2, 7, 13, and 12 sources respectively; this corresponds to detection percentages of 67%, 37%, 13%, 13%, 44%, 81%, and 75% respectively. A molecule is considered to be detected provided that (1) at least one line with a 5σ detection or two lines with 3σ detections are observed, (2) there is no confusion with common interstellar or YSO molecular lines, and (3) non-detected lines have upper limits that are consistent with the populations predicted by detected lines. Upper limit treatments are discussed subsequently in more detail. Because even the line-rich sources in our survey are line-poor in comparison to hot

[1] http://www.iram.fr/IRAMFR/GILDAS

[2] The CH_2CO transition is only available for sources in the pilot survey: B1-a, B5 IRS1, L1489 IRS, IRAS 04108, IRAS 03235, and SVS 4-5

[3] http://spec.jpl.nasa.gov

[4] http://www.astro.uni-koeln.de/cdms/catalog

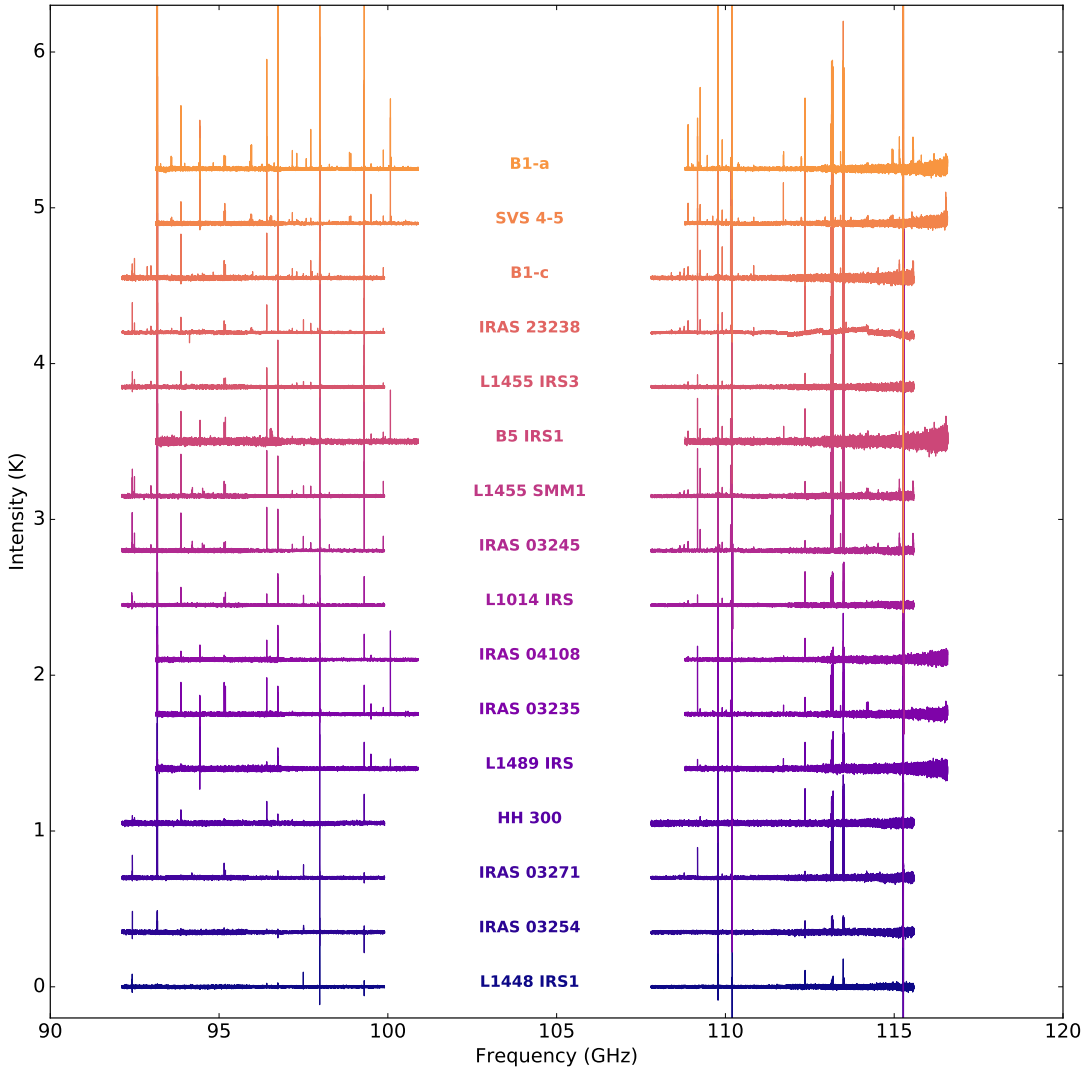

Figure 1. IRAM 30m spectra towards low-mass YSO sample, in order of line richness.

cores, overlapping lines are generally not a concern, and a single line is sufficient to claim a detection when there are no competing line identifications.

Figure 2 shows the spectral window containing the CH_3CN 6-5 ladder, with detections highlighted with a pink star. For all other molecules, spectral windows with detections are shown in the Appendix (Figures 15-20).

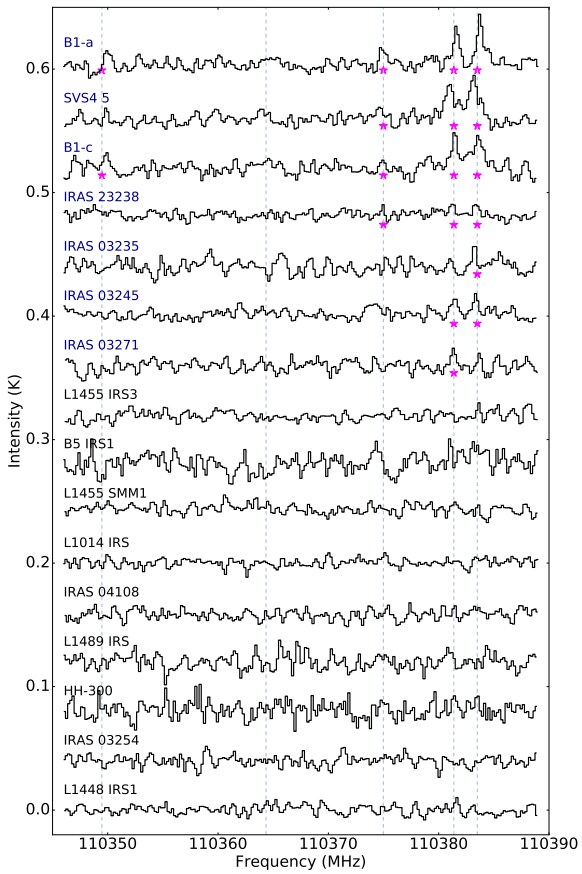

Figure 2. Blow-up of frequency range containing the CH_3CN 6-5 ladder. Grey dashed lines show the line centers, sources with positive detections are written in blue font, and individual detected lines are highlighted with a pink star.

3.2. *Rotational Diagrams*

Integrated intensities for each observed line were determined by fitting single Gaussians to each feature, and are listed in Tables 6-12 in the Appendix. For lines with substantial wings, only the central peak was used in deriving column densities. Unresolved multiplets originating from the same species were treated as a single line by combining the degeneracies and line intensities. Overlapping lines with contributions from different species were excluded from further analysis. We assume a calibration uncertainty of 10%.

For molecules with multiple line detections in a source we use rotational diagrams to calculate column densities (Goldsmith & Langer 1999). The rotational diagram for CH_3CHO is shown in Figure 3, with all additional diagrams for detected molecules in the Appendix (Figures 21-26). Tables 2 and 3 summarize the resulting column densities and rotational temperatures. Rotational diagrams from the pilot survey were refit to include additional lines that were not identified in Öberg et al. (2014).

Upper level populations for each line are calculated by:

$$\frac{N_u}{g_u} = \frac{3k \int T_{mb} dV}{8\pi^3 \nu \mu^2 S}. \quad (1)$$

Here, N_u is the column density of molecules in the upper level, g_u is the upper level degeneracy, k is Boltzmann's constant, $\int T_{mb} dV$ is the integrated main beam temperature, ν is the transition frequency, μ is the dipole moment, and S is the transition strength. Assuming optically thin lines and local thermodynamic equilibrium (LTE), each molecule's total column density N_{Tot} and rotational temperature T_{rot} in each source can be determined from:

$$\frac{N_u}{g_u} = \frac{N_{Tot}}{Q(T_{rot})} e^{-E_u/T_{rot}} \quad (2)$$

where $Q(T_{Rot})$ is the partition function and E_u is the energy of the upper level. We assume that all molecules within the beam can be described by a single temperature (e.g. Bisschop et al. 2007; Öberg et al. 2014; Fayolle et al. 2015).

For detected molecules, upper limits are calculated and included in the rotational diagrams for all listed transitions with an equal or greater transition strength and an upper level energy at most 15K greater than the detected lines. 3σ upper limits were calculated according to:

$$\sigma = \text{rms} \times \text{FWHM}/\sqrt{n_{ch}} \quad (3)$$

Here, the rms is taken from a 40 km s^{-1} spectral window containing the transition and FWHM is equal to the average FWHM of detected lines for that molecule in the same source. n_{ch} is the number of channels across the FWHM, in this case equal to ~FWHM/0.6 km s^{-1} channel^{-1}. Equation 1 is used to calculate the population upper limits.

In cases where a single transition was detected, the column densities were calculated adopting the average rotational temperatures in the sample for the species in question, if available. For HNCO and CH_2CO, at most one transition was detected for all sources. The average rotational temperature of HC_3N in our sample (14K) was used for calculating HNCO column densities and that of CH_3CHO (8K) used for calculating CH_2CO column densities. This is based on spatial trends in emission observed in high-mass protostars (Bisschop et al. 2007; Öberg et al. 2013; Fayolle et al. 2015).

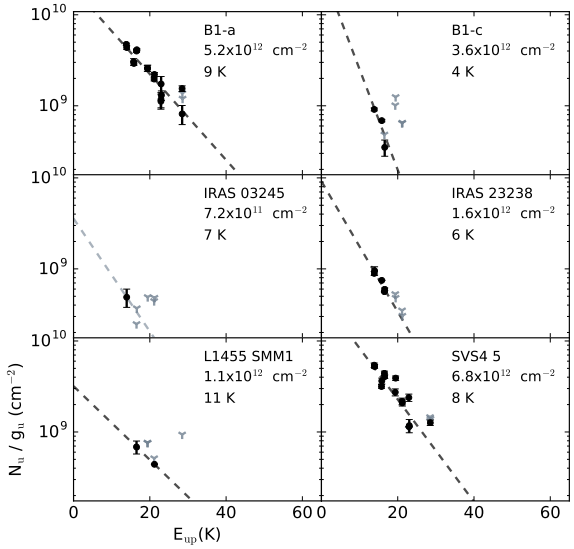

Figure 3. Rotation diagrams for CH_3CHO. Black circles indicate detections and grey triangles indicate upper limits. Black dashed lines represent the fits to the data. When a line could not be fit, a rotational temperature was assumed as described in the text, shown in grey dashed lines.

For molecules with no detected transitions in a given source, a 3σ upper limit was calculated using equation 3. In this case, the rms for each non-detected molecule was taken from a 40 km s^{-1} spectral window containing its lowest-energy transition. We assume a FWHM equal to the average FWHM of all detected lines within a given source; for sources with no detections (HH-300 and L1448 IRS1) we assume the FWHM of CH_3OH within the source. Upper limits for total column densities were calculated from equations 1 and 2 assuming the sample-averaged rotational temperatures.

We note that B1-a and B1-c appear to have a detection of CH_3CN 6_5-6_4 at 110.349 GHz, which has an upper energy of 132.8K. We exclude these points from fitting the rotational diagram. The peak velocity of this transition is slightly offset from the other CH_3CN detections for both sources in which we observe it; thus, if real this CH_3CN line does not originate from the same location as the other lines. The line may trace CH_3CN in a shock, but it is more likely due to an unidentified carrier; the latter was previously suggested by Bottinelli et al. (2007), who observed an excess of this CH_3CN transition towards the hot corino NGC1333-IRAS4B.

Table 2. Column densities and rotational temperatures: Oxygen-bearing molecules

	CH_2CO		CH_3CHO		CH_3OCH_3		CH_3OCHO	
	N_{Tot} (cm^{-2})	T_{Rot} (K)	N_{Tot}(cm^{-2})	T_{Rot} (K)	N_{Tot} (cm^{-2})	T_{Rot} (K)	N_{Tot} (cm^{-2})	T_{Rot} (K)
B1-a	8.6 (11.8) x10^{12}	*8 (2)*	5.2 (0.8) x10^{12}	9 (1)	8.1 (1.3) x10^{12}	22 (5)	5.9 (6.2) x10^{12}	17 (11)
B1-c	-	-	3.6 (3.4) x10^{12}	4 (1)	<1.0x10^{13}	*17 (5)*	<9.5x10^{12}	*16 (1)*
B5 IRS1	<1.4x10^{12}	*8 (2)*	<1.1x10^{12}	*8 (2)*	<1.0x10^{13}	*17 (5)*	<9.4x10^{12}	*16 (1)*
HH-300	-	-	<4.5x10^{11}	*8 (2)*	<7.1x10^{12}	*17 (5)*	<6.5x10^{12}	*16 (1)*
IRAS 03235	1.0 (1.4) x10^{12}	*8 (2)*	<6.1x10^{11}	*8 (2)*	<6.4x10^{12}	*17 (5)*	<4.1x10^{12}	*16 (1)*
IRAS 03245	-	-	6.4 (4.9) x10^{11}	*8 (2)*	<5.6x10^{12}	*17 (5)*	<5.8x10^{12}	*16 (1)*
IRAS 03254	-	-	<6.4x10^{11}	*8 (2)*	<8.4x10^{12}	*17 (5)*	<5.3x10^{12}	*16 (1)*
IRAS 03271	-	-	<4.8x10^{11}	*8 (2)*	<8.5x10^{12}	*17 (5)*	<4.9x10^{12}	*16 (1)*
IRAS 04108	1.4 (1.9) x10^{12}	*8 (2)*	<7.6x10^{11}	*8 (2)*	<7.2x10^{12}	*17 (5)*	<6.0x10^{12}	*16 (1)*
IRAS 23238	-	-	1.6 (1.0) x10^{12}	6 (2)	<5.1x10^{12}	*17 (5)*	<3.7x10^{12}	*16 (1)*
L1014 IRS	-	-	<3.1x10^{11}	*8 (2)*	<3.9x10^{12}	*17 (5)*	<3.2x10^{12}	*16 (1)*
L1448 IRS1	-	-	<4.2x10^{11}	*8 (2)*	<6.1x10^{12}	*17 (5)*	<4.1x10^{12}	*16 (1)*
L1455 IRS3	-	-	<4.3x10^{11}	*8 (2)*	<8.1x10^{12}	*17 (5)*	<4.8x10^{12}	*16 (1)*
L1455 SMM1	-	-	1.1 (0.3) x10^{12}	11 (7)	<6.7x10^{12}	*17 (5)*	<4.7x10^{12}	*16 (1)*
L1489 IRS	<1.4x10^{12}	*8 (2)*	<8.7x10^{11}	*8 (2)*	<8.1x10^{12}	*17 (5)*	<6.4x10^{12}	*16 (1)*
SVS4 5	9.0 (12.4) x10^{12}	*8 (2)*	6.8 (1.1) x10^{12}	8 (1)	1.2 (0.5) x10^{13}	12 (3)	7.0 (4.4) x10^{12}	15 (5)

NOTE—Uncertainties are listed in parentheses. T_{Rot} values are calculated from the rotational diagram method when possible; otherwise, sample-averaged values for that molecule are assumed, shown in italics in the table.

Table 3. Column densities and rotational temperatures: Nitrogen-bearing molecules

	CH_3CN		HC_3N		HNCO	
	N_{Tot} (cm^{-2})	T_{Rot} (K)	N_{Tot}(cm^{-2})	T_{Rot} (K)	N_{Tot} (cm^{-2})	T_{Rot} (K)
B1-a	4.9 (1.1) x10^{11}	33 (9)	4.2 (1.2) x10^{12}	12 (2)	7.7 (4.3) x10^{12}	*14 (3)*
B1-c	3.5 (0.6) x10^{11}	18 (2)	4.2 (3.4) x10^{12}	*14 (3)*	8.8 (4.9) x10^{12}	*14 (3)*
B5 IRS1	<1.7x10^{11}	*27 (7)*	3.2 (1.2) x10^{12}	11 (2)	3.5 (2.0) x10^{12}	*14 (3)*
HH-300	<1.2x10^{11}	*27 (7)*	<1.3x10^{11}	*14 (3)*	<6.6x10^{11}	*14 (3)*
IRAS 03235	1.6 (0.9) x10^{11}	*27 (7)*	3.9 (1.0) x10^{12}	13 (2)	1.8 (1.0) x10^{12}	*14 (3)*
IRAS 03245	1.9 (1.5) x10^{11}	33 (28)	3.6 (2.9) x10^{12}	*14 (3)*	2.8 (1.6) x10^{12}	*14 (3)*
IRAS 03254	<1.0x10^{11}	*27 (7)*	<9.2x10^{10}	*14 (3)*	<6.1x10^{11}	*14 (3)*
IRAS 03271	1.9 (1.1) x10^{11}	*27 (7)*	1.7 (1.4) x10^{12}	*14 (3)*	1.4 (0.8) x10^{12}	*14 (3)*
IRAS 04108	<1.2x10^{11}	*27 (7)*	<1.0x10^{11}	*14 (3)*	7.0 (4.0) x10^{11}	*14 (3)*
IRAS 23238	1.4 (0.3) x10^{11}	33 (6)	3.2 (2.6) x10^{12}	*14 (3)*	4.6 (2.6) x10^{12}	*14 (3)*
L1014 IRS	<6.2x10^{10}	*27 (7)*	4.4 (3.6) x10^{11}	*14 (3)*	1.7 (0.9) x10^{12}	*14 (3)*
L1448 IRS1	<9.4x10^{10}	*27 (7)*	<8.7x10^{10}	*14 (3)*	<4.4x10^{11}	*14 (3)*
L1455 IRS3	<9.1x10^{10}	*27 (7)*	6.5 (5.3) x10^{11}	*14 (3)*	1.7 (0.9) x10^{12}	*14 (3)*
L1455 SMM1	<1.1x10^{11}	*27 (7)*	2.4 (1.9) x10^{12}	*14 (3)*	2.4 (1.3) x10^{12}	*14 (3)*
L1489 IRS	<1.4x10^{11}	*27 (7)*	3.5 (2.4) x10^{11}	20 (13)	7.7 (4.7) x10^{11}	*14 (3)*
SVS4 5	5.2 (0.9) x10^{11}	17 (2)	1.1 (0.3) x10^{13}	13 (2)	7.0 (3.9) x10^{12}	*14 (3)*

NOTE—Uncertainties are listed in parentheses. T_{Rot} values are calculated from the rotational diagram method when possible; otherwise, sample-averaged values for that molecule are assumed, shown in italics in the table.

3.3. *Column densities and abundances*

3.3.1. *COM detections and upper limits*

Figure 4a shows the column densities derived for each molecule in all sources, both detections and upper limits. CH_3OCH_3 and CH_3OCHO are each detected in only two sources. These detections are close to the upper limits for sources without detections. Thus, the upper limits for CH_3OCH_3 and CH_3OCHO are not very constraining, and the variability in column density of these molecules cannot be well understood from this sample. All other molecules have multiple detections that are substantially larger than the non-detection upper limits, and the resulting ranges of derived column densities span at least an order of magnitude.

The sources B1-a and SVS 4-5, shown as the first and last bar in each grouping in Figure 4, stand out as being quite enhanced relative to the other sources. All 7 molecules are detected towards these sources, and the derived column densities are high compared to the sample medians. In contrast, the sources L1448 IRS1 and HH-300 have no detections. The majority of sources exhibit a range of moderate column densities, with a few but not all molecules detected in each source.

Abundances with respect to CH_3OH are shown in Figure 4b. CH_3OH column densities are taken from Graninger et al. (2016). Because column densities of CH_3OH are not available for IRAS 03254, we omit this source from comparison. Once normalized to CH_3OH, B1-a and SVS 4-5 molecule abundances are consistent or under-abundant compared with other sources, suggesting that their high column densities do not signify a distinct chemsitry.

3.3.2. *Median column densities and abundances*

Median abundances were first calculated using detections only; however, this neglects the information provided by upper limits, and thus risks over-estimating the median occurrences. Survival analysis using the Kaplan-Meier (KM) estimate of the survival function with left censorship was performed in order to account for this. In this method, all detections and non-detections are ordered, and then the values of positive detections are used to divide the total range of values into intervals. Upper limits within an interval are counted as having the lower delimiting value of the interval. In other words, each positive detection is weighted by the number of upper limits that occur between it and the next largest positive detection. Further details can be found in Feigelson & Nelson (1985) and Miller et al. (1981).

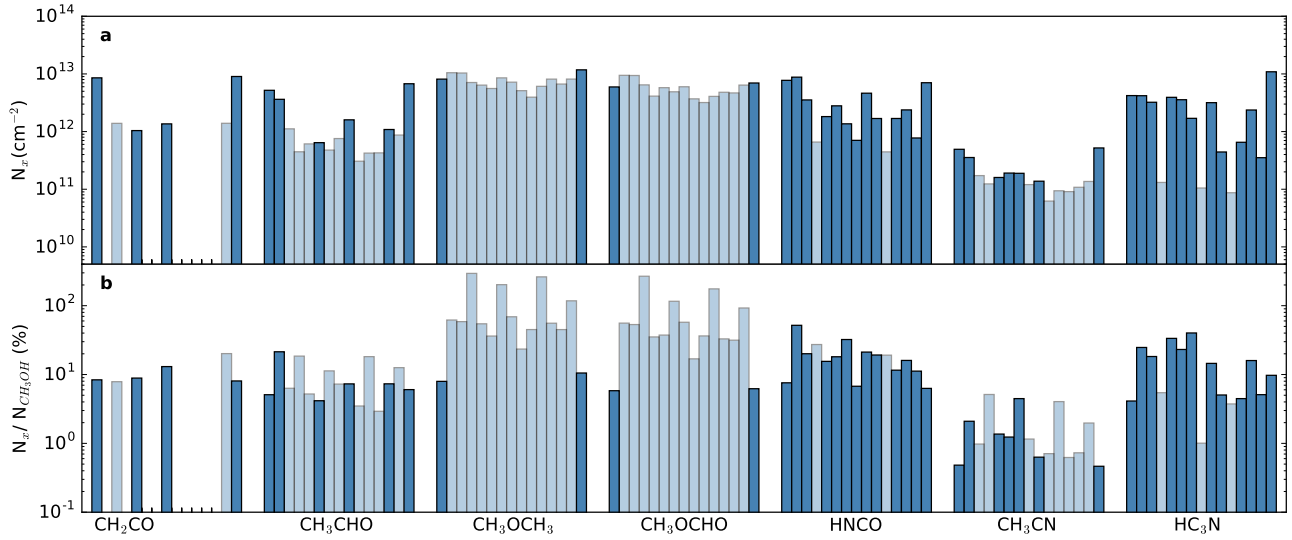

Figure 4. a: Observed column densities for each molecule. b: Abundances with respect to CH_3OH. For both panels, detections are shown in dark blue, and upper limits in light blue. For each molecule, sources are ordered alphabetically: B1-a, B1-c, B5 IRS1, HH-300, IRAS 03235, IRAS 03245, IRAS 03271, IRAS 04108, IRAS 23238, L1014 IRS, L1448 IRS1, L1455 IRS3, L1455 SMM1, L1489 IRS, SVS 4-5.

Table 4. Median column densities and abundances

	Median column densities (10^{12} cm^{-2})		Median abundances (% with respect to CH_3OH)
	Detections only	Survival analysis[a]	Survival analysis[a]
CH_2CO	5.0	$1.2\ ^{5.0}_{0.78}$	$8.2\ ^{8.8}_{7.9}$
CH_3CHO	2.6	$0.27\ ^{1.2}_{0.14}$	$4.4\ ^{6.1}_{2.3}$
CH_3OCH_3	9.9	$2.4\ ^{3.5}_{1.2}$	$5.3\ ^{9.2}_{4.0}$
CH_3OCHO	6.5	$1.9\ ^{2.9}_{1.0}$	$3.1\ ^{6.0}_{2.9}$
HNCO	2.4	$1.8\ ^{3.8}_{0.76}$	$16\ ^{20.}_{7.9}$
CH_3CN	0.19	$0.060\ ^{0.19}_{0.03}$	$0.48\ ^{1.1}_{0.46}$
HC_3N	3.2	$2.0\ ^{3.7}_{0.29}$	$7.4\ ^{20.}_{4.2}$

[a]Lower and upper quartiles shown to the right of the median

Since the survivial function is discrete, median abundances are calculated by linear interpolation between the values above and below where the cumulative density function (CDF) is equal to 0.5. However, medians cannot be computed by the KM estimate for samples with only upper limits in the lowest 50% of values since the first positive detection occurs after the cumulative density has already exceeded 0.5. In this sample, this applies to CH_3OCH_3, CH_3OCHO, and CH_3CN. To mitigate this we calculate medians using the KM estimate with the lowest value assigned a "detection" status, regardless of its true identity as a detection or a non-detection. This may result in slightly elevated estimates for median values, but as seen in Figure 5 it is still a more realistic estimate of the median than using detections only.

Median column densities for each molecule are shown in Figure 5a and Table 4 for both methods. There is a clear difference between the medians calculated from only detections and those using survival analysis, demonstrating the importance of using the constraints provided by non-detections.

Median column densities of all species except CH_3CN are on the order of 10^{12} cm^{-2}, while CH_3CN is over an order of magnitude lower. CH_3OCHO and CH_3OCH_3 have among the highest median column densities compared to the other observed molecules, but this may be somewhat misleading since each is detected in only two sources. Given the large values of the partition function for these molecules, detections are possible only for

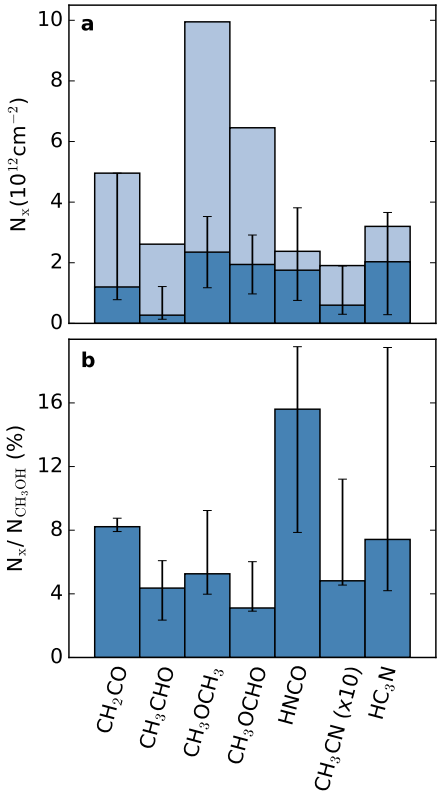

Figure 5. a: Median column densities of each molecule, calculated using detections only (light blue) and using survival analysis (dark blue). b: Abundances for each molecule calculated with survival analysis. In both panels, CH_3CN has been scaled by 10 for clarity. Error bars span the first and third quartile determined using survival analysis.

sources with very high abundances and thus the statistics are biased, even with the inclusion of upper limits. HC_3N and HNCO also have fairly high column densities and are detected in 12 and 13 sources respectively, indicating that they are both common and abundant in low-mass protostellar environments.

Median abundances using survival analysis are shown in Figure 5b. Most molecules have median abundances of a few percent with respect to CH_3OH; CH_3CN is again the exception, with a median abundance an order of magnitude lower. The distribution of abundances, reflected in the error bars spanning the lower and upper quartile, is much tighter for oxygen-bearing molecules than for nitrogen-bearing molecules; this is discussed further in the following section.

3.3.3. *Column density and abundances distributions*

To explore the distributions of column densities before and after normalization to CH_3OH, Figure 6a shows histograms of each molecule's column density. For most molecules, the range of column densities spans an order of magnitude or more. The exceptions are CH_3OCH_3 and CH_3OCHO, for which only two detections of each molecule are available. The lower and upper quartiles for column densities are listed in Table 4. HC_3N has a particularly broad distribution, with over an order of magnitude difference between the lower and upper quartile values. CH_2CO, CH_3CHO, and CH_3CN have fairly large spreads, with a factor of ∼6-7 difference in lower and upper quartile values. The narrow distributions of CH_3OCH_3 and CH_3OCHO are not informative due to the small number of detections.

When normalized to CH_3OH, the distribution of abundances of oxygen-bearing species tightens considerably as seen in the narrower distributions in Figure 6b compared to 6a, with most detections around 10% with respect to CH_3OH. In contrast, the CH_3OH-normalized abundance distributions for nitrogen-bearing species are broad. The lower and upper quartiles in Table 4 reflect this as well: for the abundances of oxygen-bearing species, upper quartile values are 1-2 times larger than lower quartile values. In contrast, upper quartile values for nitrogen-bearing species are 3-4 times larger than lower quartile values. Together, this suggests an oxygen chemistry that is connected to CH_3OH, whereas the nitrogen chemistry is regulated by other factors besides CH_3OH abundances.

3.4. *COM Rotational temperatures*

For sources with at least 3 detections of a given molecule, rotational excitation temperatures could be derived using the rotational diagram method. These spanned from 4K to 33K, with CH_3CHO having the lowest temperature and CH_3CN the highest. All rotational temperatures are quite low, indicating that the majority of emission does not come from a region that is both hot and dense. Both the temperature and density of protostars increase towards the center, therefore most emission must originate on larger scales. Since rotational temperatures depend on the excitation conditions and each molecule's excitation properties, they are typically not equal to the kinetic temperature. However, for molecules with similar dipole moments, rotational temperatures should be proportional to kinetic temperatures; for this reason we can compare CH_3CHO and CH_3CN with CH_3OH to put qualitative constraints on their emission regions. As for previous observations of low-mass (Öberg et al. 2014) and high-mass (Bisschop et al. 2007; Fayolle et al. 2015) protostars, we find a relatively low rotational temperature for CH_3CHO, suggesting that it is mainly emitting from the cold outer envelope. Likewise, we find a higher rotational temperature for CH_3CN, suggesting that it emits from closer in.

The rotational temperatures of CH_3OCH_3 and CH_3OCHO are both higher than the CH_3OH rotational temperature in the two sources in which they are detected (B1-a and SVS 4-5). Given this, it is unlikely that

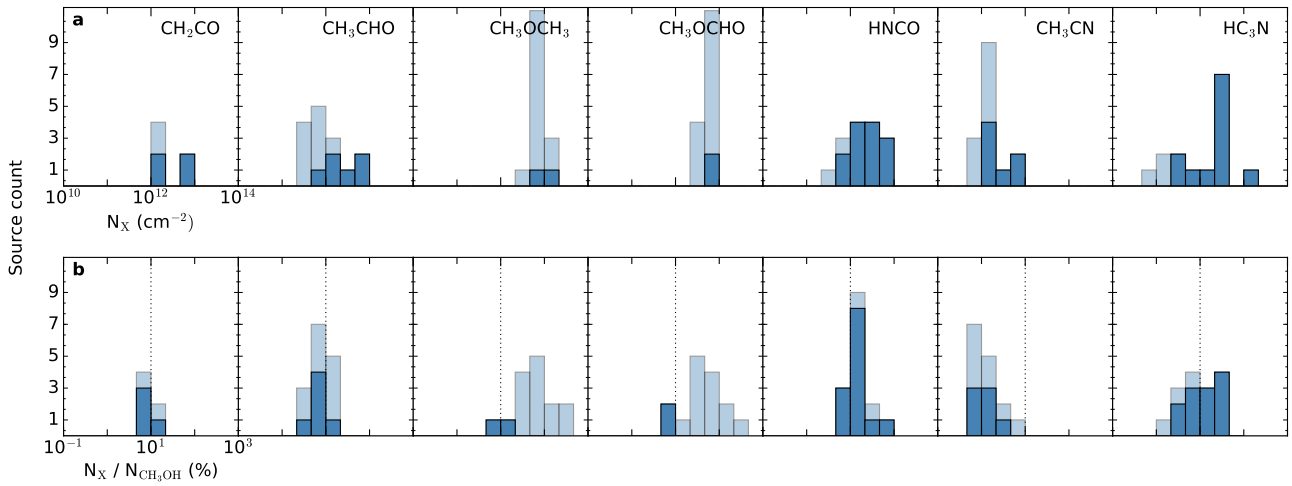

Figure 6. a: Histograms of observed column densities for each molecule. b: Abundances with respect to CH_3OH. The dotted black line represents 10%. For both panels, detections are shown in dark blue, and upper limits in light blue.

the envelope is the sole origin of emission. This is consistent with observations of hot-core MYSOs in which both molecules are classified as hot molecules (Bisschop et al. 2007). We note, however, that CH_3OCH_3 and CH_3OCHO have low signal-to-noise detections and are found only in two sources, and so further observations are required to confirm whether these molecules are indeed warm emitters in LYSOs.

3.5. *Correlation studies*

To explore chemical relationships between different COMs, we determined the correlations between each COM with one another and with CH_3OH. Strong positive correlations are expected for chemically related molecules (e.g. if one forms from another), or for molecules that depend similarly on an underlying variable such as envelope mass or temperature. When correlating column densities, some correlation is always expected since all molecules typically increase with an increasing total column density in a line of sight. This could in theory be divided out, but there are insufficient constraints on the physical characteristics of each source and on the origin of COM emission within each source to convert column densities to abundances with respect to H_2. We therefore use the column density correlation strengths to infer which molecules are more closely related, with the caveat that some of the correlation may be due to source richness rather than chemical relatedness.

We calculate Pearson correlation coefficients for each COM with one another, shown in Table 5. Only detections are used for this calculation; because of this, only pairs of molecules which are detected in at least three of the same sources have correlation coefficients listed. Figure 7 shows scatterplots of each molecule's column density plotted against one another.

Table 5. Column density correlations between molecules.

	CH_3OH	CH_2CO	CH_3CHO	CH_3CN	HC_3N
HNCO	0.69 [13]	0.98 [4]	0.79 [6]	0.79 [7]	0.67 [12]
HC_3N	0.78 [12]	0.57 [3]	0.82 [6]	0.71 [7]	
CH_3CN	0.90 [7]	0.99 [3]	0.96 [5]		
CH_3CHO	0.90 [6]	-			
CH_2CO	0.99 [4]				

NOTE—Brackets indicate the number of sources with detections for both molecules. A dash indicates a pair of molecules with fewer than 3 sources in common.

CH_3OH is well-correlated with CH_2CO, CH_3CHO, and CH_3CN, and more weakly correlated with HNCO

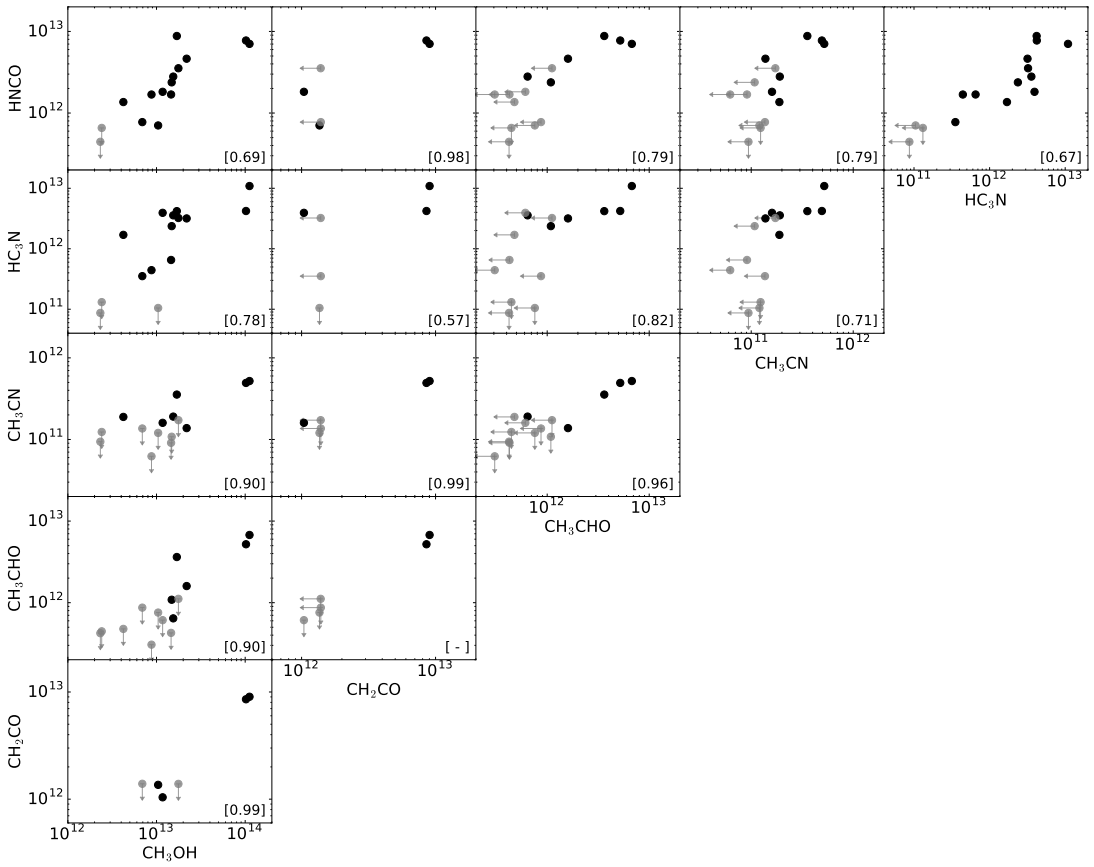

Figure 7. Column densities (cm^{-2}) of each molecule plotted against one another. Detections are shown as black circles and upper limits as grey arrows. Pearson correlation coefficients are listed in brackets.

and HC_3N. The higher correlation of CH_3OH with oxygen-bearing species compared to nitrogen-bearing species supports a scenario in which O-bearing COMs form from CH_3OH processing. Within the nitrogen-bearing family, there are no particularly strong relationships between any of the molecules. HC_3N is the least well-correlated with other molecules; this is unsurprising given that it is a carbon chain rather than a hydrogen-rich COM. CH_3OCH_3 and CH_3OCHO correlations cannot be assessed since each is detected in only two sources.

We caution that the high correlation values for CH_2CO with CH_3OH, HNCO and CH_3CN may be an artifact of the low number of CH_2CO detections: the CH_2CO transition at 100.095 GHz is only observable within the spectral range of the 6 objects in the pilot survey, of which it is detected in 4. The lack of observational constraints for intermediate values of CH_2CO hinders an interpretation of the true distribution of column densities.

Correlations of column densities with physical properties may also provide insight into the chemistry. To this end, we checked for correlations between envelope mass and bolometric luminosities (see Table 1) with our COM column densities.

All molecules correlate positively with envelope mass (Figure 8). This is in part because more molecules are present in lines of sight containing more material. The correlation is strongest for HC_3N followed by HNCO, with all other molecules showing weaker positive correlations. Among the nitrogen-bearing species, the observed sequence of correlation strengths with M_{env} are consistent with the expected origin of emission of each molecule. HC_3N is thought to form through gas-phase chemistry and emit from the cold envelope, and therefore should trace the envelope mass very well. HNCO is thought to emit from both the warm inner region and the cold envelope, which is consistent with a weaker correlation with envelope mass. Based on its rotational temperature, CH_3CN is mainly present in the warmer, more compact region of the protostar, and should therefore not depend strongly on total envelope mass.

Interestingly, CH_3CHO and CH_2CO are also cold emitters, but unlike HC_3N they depend only weakly on envelope mass. This could be because these molecules form mainly on grain surfaces rather than via gas-phase chemistry.

Correlations with bolometric luminosity are also pos-

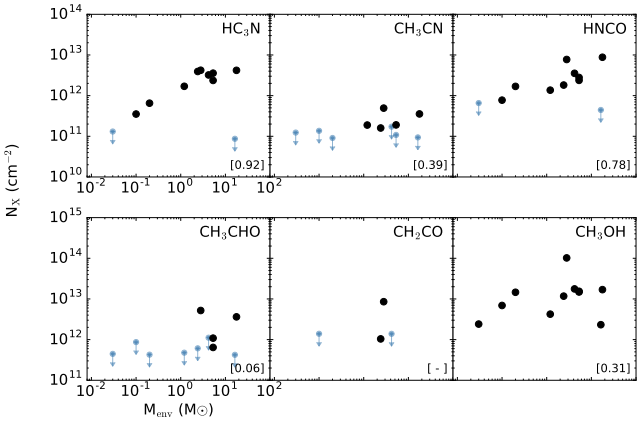

Figure 8. Column densities plotted against envelope mass. Upper limits due to molecule non-detections are shown in blue. Pearson correlation coefficients are shown in brackets in the lower right corner.

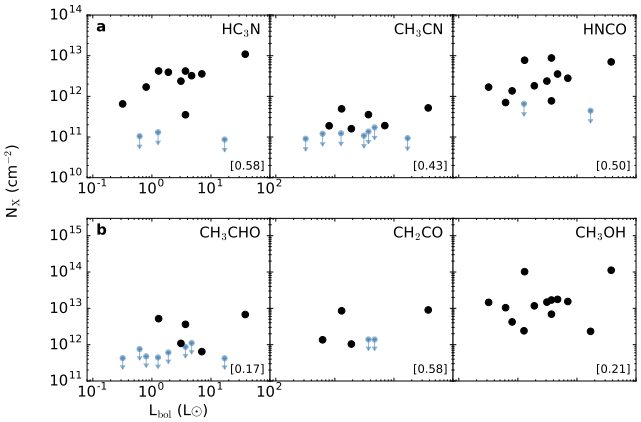

Figure 9. Column densities plotted against bolometric luminosity. Upper limits due to molecule non-detections. Pearson correlation coefficients are shown in brackets in the lower right corner.

itive, shown in Figure 9. In contrast to the envelope mass correlations, no single molecule stands out as particularly well-correlated with L_{bol}. This suggests that the weak correlations are not driven by chemistry, but rather excess excitation and ice desorption (affecting all molecules) around hotter protostars. The most obvious outlier in Figures 8 and 9 is L1448 IRS1, towards which no COMs are detected despite being one of the most massive and luminous of our sample. Massive sources are more likely to be young sources (e.g. Hatchell et al. 2007), so its unusual characteristics could be related to an early evolutionary stage.

All sources in the sample have been detected in water ice and in at least one of the minor ice constituents NH_3, CH_3OH, and CH_4 (see Table 1). In the context of COM formation, it is especially interesting to test whether the relative abundances of O- and N-bearing COMs are related to the relative ice abundances of CH_3OH (the theoretical starting point of O-rich COM

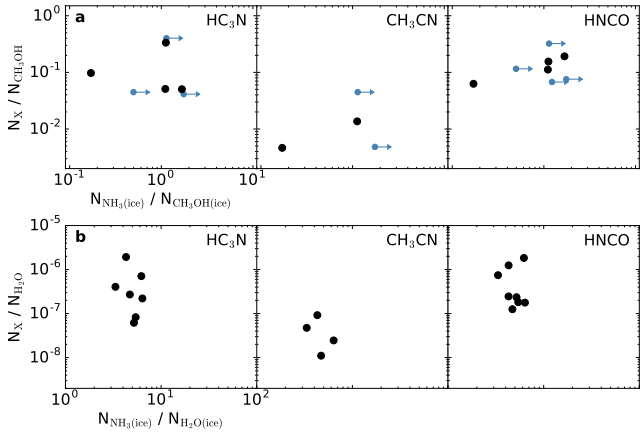

Figure 10. (a): Abundances with respect to CH_3OH for the nitrogen-bearing species plotted against the observed NH_3/CH_3OH ice ratio. Lower limits due to non-detections of CH_3OH ice are shown in blue. (b): Abundances with respect to H_2O for the nitrogen-bearing species plotted against the observed NH_3/H_2O ice ratio.

chemistry) and NH_3 (the main observed carrier of nitrogen in interstellar ices (Öberg et al. 2011a); N_2 is also a possible reservoir of nitrogen in ices but cannot be observed directly). The number of sources with both CH_3OH and NH_3 detections is unfortunately small: only 10 sources have both detections, or one detection and one low upper limit, for CH_3OH and NH_3 ice columns. Of this, only a subset are rich in COMs, which limits the conclusiveness of any correlation studies. Figure 10a shows the abundances with respect to CH_3OH gas for the nitrogen-bearing species, plotted against the NH_3/CH_3OH ice ratio towards the same sources. HC_3N/CH_3OH gas-phase ratios are clearly not correlated with NH_3/CH_3OH ice ratios. Otherwise, there are no conclusive relationships between the abundance of NH_3 ice and nitrogen-bearing molecules in this sample. At first glace, CH_3CN/CH_3OH and $HNCO/CH_3OH$ appear correlated with NH_3/CH_3OH ice ratios; however, the presence of lower limit outliers, one for CH_3CN and two for HNCO, suggests that the complex cyanide chemistry may be only weakly dependent on NH_3 ice abundances or altogether independent. Further ice observations may reveal these lower limits to be anomalous, or may reveal relationships between other nitrogen-bearing molecules and NH_3 ice. Figure 10b shows the abundances with respect to H_2O instead of CH_3OH for NH_3 ice verses gas-phase nitrogen-bearing species. Again there is no obvious relationship, indicating that the lack of dependency of cyanide chemistry on NH_3 is not an artifact of the normalizing species.

4. CHEMICAL MODEL

4.1. *Model description*

In order to compare our observational results for LYSO chemical abundances with current theoretical predictions, we have used the three-phase chemical kinetics code MAGICKAL (Garrod 2013) to simulate LYSO chemistry. The model version and the chemical network employed are those presented by Garrod et al. (2017); however, for the molecules of interest here, the differences between the work of Garrod (2013) and more recent implementions are very minor. The model considers both the gas-phase and grain-surface/ice-mantle formation and destruction of molecules. Complex organic molecules are largely assumed to have only dust grain-related formation mechanisms, in the absence of other information.

We run the model multiple times using a selection of physical conditions that are representative of values at a range of radial distances from the core center. We use results from this grid of chemical models to produce a composite, spatially-dependent picture of the chemistry in the LYSO.

We begin with a spherically symmetric physical model of a generic LYSO, with a power-law temperature profile adapted from Chandler & Richer (2000):

$$T(r) = 60\left(\frac{r}{2\text{x}10^{15}\text{m}}\right)^{-q}\left(\frac{L_{bol}}{10^5 L_\odot}\right)^{q/2}\text{K}, \qquad (4)$$

where we assume $q = 2/5$ and L_{bol} is either 1 or 10 $L_\odot$. For the density profile, we assume the power law:

$$n_H(r) = n_{1000AU}\left(\frac{r}{1000AU}\right)^{-\alpha}. \qquad (5)$$

Based on the median values determined from radiative transfer modeling of low-mass protostars in Jørgensen et al. (2002), we assume $n_{1000AU} = 10^6$ cm^{-3} and $\alpha = 1.5$. We also assume an inner radius where T = 250K, again following Jørgensen et al. (2002), and an outer radius where T = 10K. In the $L_{bol} = 10$ $L_\odot$ case, a temperature of 250K is achieved at a radius of 3.8 AU, with a corresponding density of 4.27×10^9 cm^{-3} at that position. In the $L_{bol} = 1$ $L_\odot$ case, the peak temperature of 250K corresponds to a radius of 1.2 AU, at which a density of 2.89×10^{10} cm^{-3} is achieved. The latter value is taken as the maximum density for which chemical-model data are required (in either luminosity case).

To populate the radial density profile with chemical data, we determine a total of 51 densities for which models are to be run, ranging logarithmically from the maximum of 2.89×10^{10} cm^{-3} down to 3.45×10^4 cm^{-3}. For each of these densities, we run a dedicated hot-core type model, using a two-stage approach (following Garrod 2013): stage one consists of an isothermal collapse from density 3000 cm^{-3} up to the final density chosen for that run; in stage two, this density is fixed and the gas and dust temperatures gradually rise to a maximum of 400K, using the "intermediate" warm-up timescale (which goes from 8 – 200K in 2×10^5 yr, producing a total warm-up timescale from 8 – 400K of 2.85×10^5 yr).

For either the $L_{bol} = 1$ $L_\odot$ or 10 $L_\odot$ case, models with densities that fall within the maximum and miminum values are chosen and placed at the appropriate radius. Then, from within each model, the abundances of all simulated molecules are extracted according to the instantaneous temperature achieved during warm-up, as determined by the temperature profile at that specific radius. To obtain data at the precise temperatures required, the model output data are interpolated between output temperature values; the temperature resolution obtained in the models is always less than 1% of the absolute value.

In this way, each model placed at a specific position in the density profile is fixed in time according to the local temperature. To account for uncertainties in the temperature profile, we also extract chemical profiles corresponding to local temperature values that are 10% lower and 10% higher temperatures than those given by the fiducial temperature profile in equation 4.

The resulting radial profiles for all molecules are then used to calculate the line-of-sight column densities that would be observed with a single-dish telescope. To do so, we convolve the molecular abundance $\frac{n_X}{n_H}(r)$, hydrogen density $n_H(r)$, and emitting area $A(r)$ at each radius. We then integrate this from our minimum to maximum radii to yield the total number of molecules of a given species within the beam:

$$n_X = \int_{r_{min}}^{r_{max}} A(r) n_H(r) \frac{n_X}{n_H}(r). \qquad (6)$$

The column density is then simply:

$$N_X = \frac{n_X}{\pi r_b^2}, \qquad (7)$$

where r_b is the beam radius. We assume a 10" beam radius based on the size of the observing beam (Section 2), and a distance to the model protostar of 200pc. In order to account for the cylindrical line of sight, we express $A(r)$ as:

$$A(r) = \begin{cases} 4\pi r^2, & \text{if } r \le r_b \\ 2\pi[r_b^2 + \left(r - \sqrt{r^2 - r_b^2}\right)^2], & \text{if } r > r_b \end{cases} \qquad (8)$$

In other words, while the radius is smaller than the beam radius, the emitting surface corresponds to the surface area of a sphere at that radius. Beyond the beam radius, the emitting surface consists of spherical caps in front of and behind a sphere of radius = r_b. These caps have a constant fixed base radius r_b and a height that varies depending on the radius. Figure 11 illustrates how this

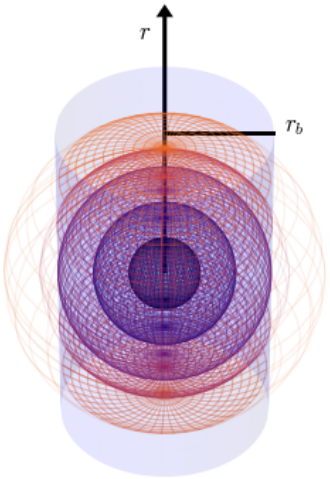

Figure 11. Schematic of emitting surfaces contained within a cylindrical beam for different radial shells.

treatment accounts for material in the line of sight while excluding material outside the beam.

Our use of a single warm-up timescale keeps the model grid to a manageable size. The choice to use the "intermediate" timescale is based on its ability to best reproduce the abundances of hot-core type molecules at the high temperatures of such sources. In the case of the low-mass protostars that concern this work, the "fast" timescale could also be an appropriate choice; however, the differences between the "fast" and "intermediate" results are mainly quantitative rather than qualitative (in contrast with the "slow" warm-up timescale models). Differences between peak abundances calculated by these models are likely to be on the order of a factor of a few. Such variations are acceptable in the context of our generic model, but the modeling of specific sources in the future may be tailored to more specific warm-up timescales, using an explicitly determined infall speed.

4.2. *Model results*

Figure 12 shows the 1D radial profiles of COM fractional abundances for both the $1L_\odot$ and $10L_\odot$ protostar simulations. The variations in temperature by $\pm 10\%$ do not produce significant changes in the peak abundances; rather, they alter the radial onset of peak values, thereby changing the calculated column densities. Generally, trends in the radial abundances are consistent with our expectations based on observations: CH_3OCH_3 and CH_3OCHO, which are thought to emit from warm inner regions of the protostar, drop off in abundance moving to larger radii, while the "cold" emitters CH_2CO, CH_3CHO, HC_3N, and HNCO maintain a high abundance at all radii. Interestingly, CH_3CN has a profile more similar to the cold emitters despite its observationally derived warmer rotational temperature. We discuss the chemistry of these models further in Section 5.2.

5. DISCUSSION

5.1. *COM formation chemistry*

Correlations among COMs and between COMs and source properties provide constraints on their chemistry. In this subsection, we discuss the formation chemistry of individual molecules based on their rotational temperatures and observed correlations with CH_3OH, protostellar properties, and ice abundances (Figures 7-10).

CH_2CO: CH_2CO formation has been demonstrated experimentally by ice processing, with proposed formation mechanisms of either C_2O hydrogenation (Maity et al. 2014) or vinyl alcohol formation and decomposition (Hudson & Loeffler 2013). However, theory indicates that H addition to C_2O is the dominant pathway (Garrod et al. 2008). The strong correlation of CH_2CO with CH_3OH along with its low rotational temperature suggest that ketene forms via atom addition reactions in simple ices (i.e. CO + C $\rightarrow$ C_2O, followed by hydrogenation to CH_2CO) similar to CH_3OH formation.

CH_3CHO: CH_3CHO also correlates strongly with CH_3OH. CH_3CHO has a very low excitation temperature (8K) and is therefore likely a zeroth or first-generation COM. As mentioned in Section 3.5, CH_3CHO does not correlate well with M_{env}; this is in contrast to the gas-phase chemistry product HC_3N. CH_3CHO is therefore not likely to be a gas-phase product. Both experiments (Bennett et al. 2005; Öberg et al. 2009) and modeling (Garrod et al. 2008) demonstrate efficient formation of acetaldehyde from radical products of CH_3OH, namely CH_3 and HCO. CH_3OH processing is not the only pathway to CH_3CHO (CH_3 can also be derived from the dissociation of CH_4, and the HCO radical can form from CO hydrogenation or dissociation of H_2CO), but the tight correlation suggests that CH_3OH is an important precursor to CH_3CHO

CH_3OCH_3 and CH_3OCHO: Methyl formate and dimethyl ether have fairly warm rotational temperatures in our survey, with averages of 17K and 16K, respectively. This is much warmer than CH_3CHO, suggesting that these molecules originate closer to the central protostar. Both molecules are thought to form from recombinations of radical products of methanol, and our data is consistent with this formation scenario: CH_3OCH_3 and CH_3OCHO are the most abundant towards sources with high CH_3OH column densities. However, with only two detections this cannot be ascertained with any confidence. Firm detections in sources with lower column densities will help to elucidate this relationship. We note that this will likely require ALMA observations, as the observations presented here are already quite deep. Spatially resolved observations towards the sources with

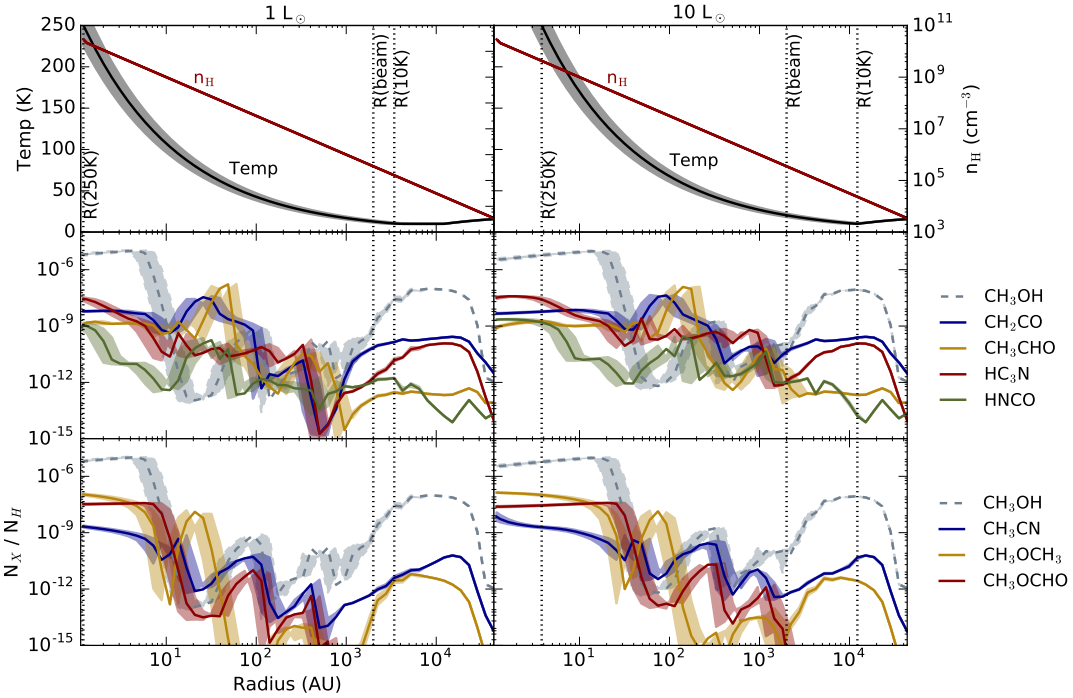

Figure 12. Chemical models for $1L_{\odot}$ and $10L_{\odot}$ LYSO simulations. In all panels, dotted vertical lines mark the inner radius at 250K, the beam radius of 10" for an object at 200pc, and the outer radius for a 10K cutoff temperature. The shaded regions around each line represent results from temperature profiles 10% higher and 10% lower than the fiducial run. Top panels: temperature and density profiles (equations 4 and 5). Middle panels: fractional abundances of the typically "cold" emitters CH_2CO, CH_3CHO, HC_3N, and HNCO. Bottom panels: abundances of the typically "warm" emitters CH_3CN, CH_3OCH_3, and CH_3OCHO. CH_3OH is shown for comparison in both the middle and bottom panels.

detections would also be helpful in constraining the formation chemistry.

HNCO: The chemical origin of HNCO is still not particularly well understood. Recent experiments have shown that HNCO can be produced in ices from CO reacting with NH radicals before N is fully hydrogenated to NH_3 (Fedoseev et al. 2015), or from simultaneous UV irradiation and hydrogenation of NO in CO, H_2CO, and CH_3OH ices (Fedoseev et al. 2016). Modeling by Garrod et al. (2008) shows that HNCO formation is efficient only by the gas-phase destruction of more complex grain-surface products, urea in particular. However, the recent model of Belloche et al. (2017) suggests reaction between NH and CO may be efficient (see Section 5.2). Several aspects of our HNCO observations support a scenario in which HNCO mainly forms through atom addition ice chemistry in the cold envelope. First, the ubiquity of HNCO in our sources favors an early formation (i.e. zeroth-generation COM chemistry): its detection towards sources with no other detections precludes a formation chemistry dependent on high gas-phase abundances of large complex molecules (i.e. second-generation formation). Moreover, HNCO correlates relatively well with envelope mass, indicative of formation in the envelope. Finally, HNCO column densities are fairly well correlated with CH_3OH for sources with low column densities of CH_3OH, but the two sources with much higher CH_3OH column densities (B1-a and SVS 4-5) do not display a comparable increase in HNCO column density. This is consistent with a scenario of co-formation of HNCO and CH_3OH in the cold envelope, while HNCO destruction in the core region could explain the saturation behavior.

CH_3CN: CH_3CN has the highest rotational temperature of all the COMs observed, with an average of 27K; together with the lack of correlation between CH_3CN and M_{env}, this suggests a more centrally concentrated emission origin and an efficient "lukewarm" pathway to CH_3CN. In hot cores, CH_3CN is thought to form mainly on grain surfaces through recombination of CH_3 + CN, followed by sublimation above ∼90K (Garrod et al. 2008). A gas-phase channel, involving HCN + $CH_3^+ \rightarrow$ CH_3CNH^+ followed by $CH_3CNH^+ + e^- \rightarrow CH_3CN$ + H, may become important at lower temperatures. In our sample, CH_3CN correlates well with CH_3OH, indicating that these molecules have similar underlying chemistries and therefore that ice chemistry may be important in CH_3CN formation. However, as discussed in Section 5.2, the chemical model relies on gas-phase chemistry to efficiently form CH_3CN at these temperatures. Thus, there is some tension between the model and observations in inferring the dominant CH_3CN formation channel. Fi-

nally, CH_3CN has no obvious correlation with the NH_3 ice column, indicating that cyanide production in the ice is not linked to NH_3.

HC_3N: HC_3N has the most scatter of any molecule in its correlation with CH_3OH. This is unsurprising given that cyanopolyyne observations can be well-reproduced by purely gas-phase models (Herbst & van Dishoeck 2009); any correlation with CH_3OH is likely related to the scale of the object and not a reliance on CH_3OH chemistry. This is also consistent with the weak correlation of HC_3N with all other COMs, discussed in Section 3.5. The tight correlation between envelope mass and HC_3N abundance and the obvious lack of correlation with NH_3 ice further support this. These observations support the general notion that hydrocarbon species are mainly gas-phase products, and do not require grain-surface chemistry to explain their abundances. Interestingly, Graninger et al. (2016) found a positive correlation between the carbon chain C_4H and CH_3OH in these LYSOs; this suggests that nitrogen-bearing carbon chains have distinct gas-phase formation chemistries from unsubstituted carbon chains.

5.2. *Modeled vs. observed chemistry*

Figure 13a compares beam-averaged COM abundances with respect to CH_3OH for our observations and modeling results (Section 4). For the observations, median values are shown as pink stars, with error bars spanning the first and third quartile. For the model, we show results from both $1L_\odot$ (light blue) and $10L_\odot$ (dark blue) temperature profiles. Triangles represents results from the fiducial temperature profiles, and error bars show the results for temperature profiles 10% higher and 10% lower.

Apart from HNCO, the model abundances are within an order of magnitude of the observations. Agreement within an order of magnitude is very reasonable given modeling uncertainties in the reaction rates as well as observational uncertainties in the different excitation properties of the molecules being compared. In particular, the systematic underestimation of most molecules by the model may be due in part to an excess of CH_3OH in the model at large radii, caused by overactive chemical desorption of methanol at cold temperatures. The underproduction of HNCO by several orders of magnitude is likely a result of an over-estimated barrier for the grain surface process of NH + CO → HNCO, which impedes efficient grain-surface formation of HNCO in the model. While there are no strong constraints on this barrier from laboratory work, recent modeling work by Belloche et al. (2017) tested several values ranging from 1000 – 2500K, the latter value being the one used in our present study. They found that the barrier is required to be no greater than ∼1500K in order to produce sufficient

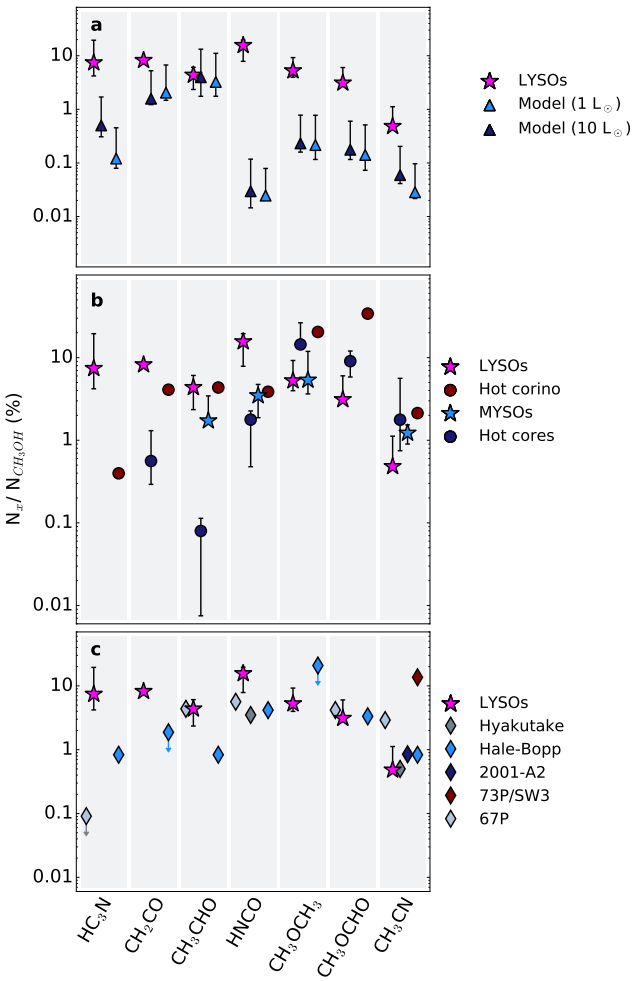

Figure 13. COM abundances with respect to CH_3OH across different types of objects. For all panels, LYSOs are shown as pink stars. Scatterpoints represent median values and error bars span the first and third quartile. a: Comparison with abundances from the protostellar warm-up model described in Section 4 for 1 $L_\odot$ (light blue) and 10 $L_\odot$ (dark blue) profiles. Error bars span the results for temperature profiles 10% higher and 10% lower than the fiducial run. b: Comparison of different star formation environments. Hot corinos (van Dishoeck et al. 1995; Cazaux et al. 2003) are shown in dark pink; MYSOs (Fayolle et al. 2015) in light blue; and hot cores (Bisschop et al. 2007) in dark blue. c: Comparison with observations of solar system comets (Crovisier et al. 2004; Mumma & Charnley 2011; Goesmann et al. 2015).

HNCO to explain observed abundances of CH_3NCO. The value of around 2500K used in the present model was adopted by Garrod et al. (2008), when this reaction was first introduced into the network, and was based on the barrier found for the analogous reaction H + CO → HCO. Reducing the current value of 2500K to the 1500K recommended by Belloche et al. may therefore improve agreement with our observational data in future model iterations.

Figure 14 shows the fraction of each molecule's total column density coming from different temperature

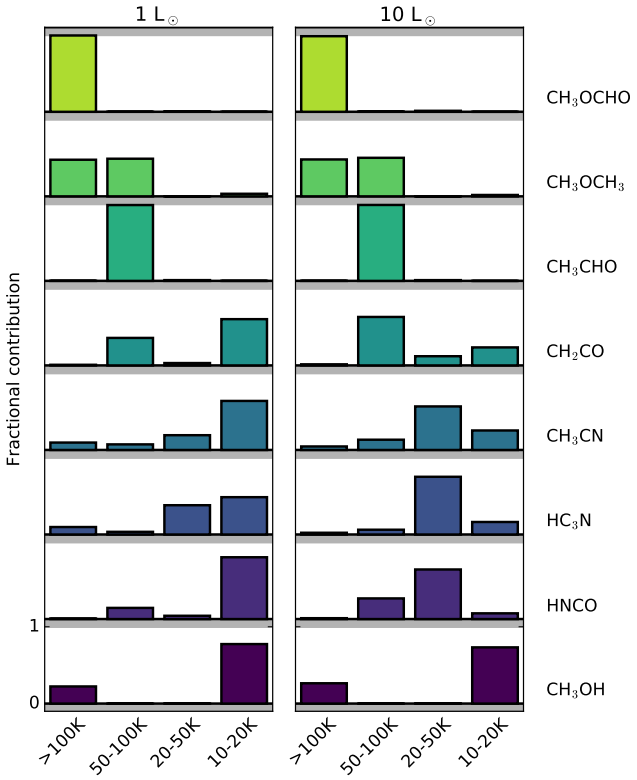

Figure 14. Model results showing the fraction of each molecule's total column density that comes from different temperature ranges. For each molecule, the y scale is the same as is indicated for CH_3OH.

ranges in the model, which can be compared with measured rotational temperatures. We note that if the observed line transitions are not in LTE then the measured rotational temperatures will underestimate the kinetic temperature. To assess how much this impacts our observations, we run RADEX models for molecules with both collisional constants and rotational temperatures (HC_3N, CH_3CN, and CH_3OH; van der Tak et al. 2007) using the measured rotational temperatures and column densities as inputs and assuming the density and temperature profiles in Section 4.1. We find that CH_3CN and HC_3N observations are well reproduced by the simulated RADEX emission while CH_3OH is not. Therefore, for some molecules (especially oxygen-bearing species), the measured rotational temperatures and column densities may be affected by non-LTE effects.

We also estimate the temperature above which HC_3N, CH_3CN, and CH_3OH should be in LTE. This is done using the collisional constants for these molecules (Schöier et al. 2005), again assuming the model density and temperature profiles. We find that most lines transition to non-LTE conditions at densities corresponding to 10-25K. Most molecules have observed rotational temperatures around or below this range; this suggests that at least some component of our observed emission is subthermal, consistent with the RADEX results. Therefore, in comparing with the model emission temperatures, we emphasize that the measured rotational temperatures should be regarded as broadly corresponding to inner, outer, and intermediate emission origins, and likely do not correspond exactly to the actual kinetic temperature.

CH_3OCHO and CH_3OCH_3 are both found at warm to hot temperatures (>50K) in the model, compared with rotational temperatures of 16K and 17K, respectively. However, these molecules are detected towards only 2 sources, and only in a few detected lines, so it is difficult to assess how serious these constraints are. They seem to rule out, however, that the emission is coming exclusively from the hot material as predicted by the model. HC_3N, HNCO, CH_2CO, and CH_3CN are all dominated by temperatures colder than 50K in the model. The available rotational temperatures (14K for HC_3N and 27K for CH_3CN) are fully consistent with this. Thus, the model successfully reproduces the envelope-dominated, low-temperature chemistry seen in these LYSOs, without the need for hot-core chemistry. This is true even for CH_3CN, which is typically considered a hot core molecule. The gas-phase pathway described in Section 5.1 is mainly responsible for this lukewarm formation in the model, and is driven by an enhancement of gas-phase HCN. This in turn is due to either sublimation of HCN from grains in warmer regimes (∼40K), or purely gas-phase HCN formation in cooler regimes. The observed rotational temperature of 27 K is consistent with some combination of low and intermediate temperature production of CH_3CN.

CH_3CHO is found entirely at warm temperatures (50-100K) in the model due to desorption of CH_3CHO formed on grain surfaces; this is much higher than its observed 8K rotational temperature. Unlike methyl formate and dimethyl ether, acetaldehyde has very well-populated rotational diagrams and therefore the rotational temperature is more secure. It seems, then, that the observed CH_3CHO is being produced through some cold formation pathway other than the radical recombination chemistry included in the model.

The majority of CH_3OH in the model is found at cold temperatures (10-20K). Cold CH_3OH in the model is likely somewhat over-abundant due to an overactive chemical desorption, contributing to the systematic under-estimation of other COM abundances seen in Figure 13. Even so, observational rotational temperatures for CH_3OH in these sources are ∼5-6K (Graninger et al. 2016), consistent with a mainly cold origin. This suggests that while the magnitude of cold CH_3OH in the model may be too high, the trend of dominantly cold emission is appropriate.

The high efficiency of cold chemical desorption of

methanol is a result of the rapid abstraction of hydrogen from methanol by H atoms, followed by re-hydrogenation by another H atom. Chemical desorption occurs in 0.24 % of re-hydrogenation cases, as determined by the method of Garrod et al. (2007), using an efficiency factor $a = 0.01$. The abstraction and re-hydrogenation of methanol on the grains in this model is sufficiently fast to produce an excess of gas-phase methanol, while the total remaining on the grains is affected only to a relatively small degree. The CO-H_2CO-CH_3OH system on grains is complex, with reactions that allow inter-conversion in both directions. The barriers and branching ratios for many of these processes are poorly-defined. The return of grain surface-formed methanol to the gas phase is therefore a function of both its formation/re-formation on grains and the efficiency of desorption, which is also poorly constrained.

In addition to gas-phase abundances, the model also provides ice abundances. In practice, observations of ices are made in absorbance and therefore trace a pencil beam of protostellar material rather than the entire envelope. To compare with observed ice column densities, therefore, the number density of each ice species in the model is simply integrated out to the maximum radius. The model produces fairly consistent values with the measured ice columns in Table 1, with H_2O column densities on the order 10^{19}cm^{-2} compared with observed values of 10^{18}-10^{19}cm^{-2}. CH_3OH model ice abundances with respect to water are around 7%, which is consistent within a factor of a few of measured values, while NH_3 model abundances of 19% are somewhat high compared to observations.

In the model, the number densities of ice species peak just outside of the ice sublimation line around 130K, corresponding to 6AU in the $1L_\odot$ case and 21AU in the $10L_\odot$ case. This is a much smaller spatial scale than our gas-phase observations, and therefore ice absorption measurements are likely not probing the same radius as the gas-phase observations. Nonetheless, observed gas and ice abundances should still be related for molecules that form primarily in the ice phase, assuming that ice compositions do not evolve substantially between the outer and inner envelope. Indeed, in the model the ice abundance profiles are essentially flat from the 10K radius in to the sublimation line. Ices observed in absorption close to the sublimation line should therefore preserve a similar composition to ices in the outer envelope, from which many of the observed gas-phase COMs likely originate.

5.3. *Massive vs. low-mass protostellar chemistry*

We next compare observations of COMs towards different types of protostars. We consider our sample of low-mass protostars without clear evidence for hot corinos (subsequently termed LYSOs), the hot corino source IRAS 16293-2422, and analogously high-mass protostars without and with hot cores (termed MYSOs and hot cores, respectively). Abundance measurements for the hot corino are taken from van Dishoeck et al. (1995) and Cazaux et al. (2003); the MYSO sample is from Fayolle et al. (2015); and the hot-core sample is from Bisschop et al. (2007). Survival analysis was performed on the MYSO and hot-core samples in order to derive median values accounting for upper limits in these surveys.

We adopt beam-averaged abundances with respect to CH_3OH under the assumption that the COMs and CH_3OH have the same distributions (Herbst & van Dishoeck 2009; Öberg et al. 2011b). This may not be an appropriate assumption, particularly for centrally concentrated warm emitters, but a lack of consistent structural information for the different sources prevents a more thorough treatment of beam dilution. There are some uncertainties then in the abundances with respect to CH_3OH due to potential differences in the emission origin of each COM.

We now compare our LYSO sample with the hot corino IRAS 16293. We note that the LYSO sources in our survey could potentially host hot corinos, however our observations are not sensitive to this emission. The maximum observed transition energy of ∼40K as well as the exclusion of line wings from spectral fitting support that the molecules observed are emitting from the outer regions of the protostar. Compared with IRAS 16293, the LYSOs are enhanced in the carbon chain HC_3N, comparable or slightly enhanced in the cold COMs CH_2CO, CH_3CHO, and HNCO, and underabundant in the hot COMS CH_3CN, CH_3OCH_3, and CH_3OCHO. This suggests an evolutionary sequence that results in the appearance of a central brightly emitting hot corino without destroying the envelope COM chemistry. We note that IRAS 16293 may not be representative of typical hot corino abundances, and a larger sample of these objects is required to make firm comparisons.

The MYSOs in Fayolle et al. (2015) have large envelopes with ice detections and lack a central hot core, and should therefore represent a comparable evolutionary stage to our LYSO sample. LYSOs have slightly higher abundances relative to MYSOs of the cold molecules CH_3CHO and HNCO, and comparable abundances for the warm molecules CH_3OCH_3 and CH_3CN. Overall, the chemistries of these types of objects appear very similar, with slight enhancements of cold molecules in the LYSOs that could be attributed to the generally colder temperatures of low-mass protostars.

It has been previously noted that hot corinos of LYSOs have abundances comparable to or greater than hot cores (e.g Bottinelli et al. 2007; Herbst & van Dishoeck

2009). While this is true for IRAS 16293, we note that from our unbiased sample of LYSOs this is clearly not typical for all low-mass objects. Furthermore, generalizing COMs as a single category seems to be an overly reductive classification, as cold and hot molecules represent distinct chemistries, and their emission trends between environments may differ.

5.4. *Comparisons with solar system chemistry*

Finally, we compare LYSO median abundances with observations of solar system comets (Crovisier et al. 2004; Mumma & Charnley 2011; Goesmann et al. 2015). In Figure 13c, most cometary abundances appear consistent with LYSO abundances, with the exception of HC_3N and CH_2CO. Since LYSOs represent regions of solar-type star formation, this similarity supports the notion that (1) the solar system is fairly typical in its chemistry, and other sun-like stars should have similar chemical inventories; and (2) chemistry early in the evolution of a star is propagated through later stages. This suggests that some of the comet's molecular composition is inherited from the early stages of star formation.

HC_3N and CH_2CO are each about an order of magnitude higher in LYSOs than in comets. The formation mechanisms discussed in Section 5.1 suggest that it may be difficult to form these molecules at later evolutionary stages: HC_3N is a dominantly gas-phase product favored by the low-density, cold outer envelope, while CH_2CO is thought to form early via atom addition in simple ices. Both of these are also unsaturated molecules that are susceptible to depletion via hydrogenation or photoprocessing. This is in contrast to CH_3CHO and HNCO, which are also unsaturated but have formation channels involving radical recombinations that can continue at later stages of disk and planet formation.

6. CONCLUSIONS

Based on a survey of complex organic molecules towards 16 young low-mass protostars using the IRAM 30m telescope, we conclude the following:

1. The molecules CH_2CO, CH_3CHO, CH_3OCH_3, CH_3OCHO, HC_3N, and HNCO all have median column densities on the order of 10^{12} cm^{-2} and median abundances with respect to CH_3OH around five to ten percent. CH_3CN is an order of magnitude lower in column density and abundance.

2. For this sample of LYSOs at similar evolutionary stages, COM column densities span at least an order of magnitude. The distribution is reduced, especially for oxygen-bearing molecules, upon normalizaiton to CH_3OH.

3. Our findings are consistent with grain-surface chemistry as the dominant formation pathway to most COMs in this survey. There is evidence that the complex organics either form from or co-form with CH_3OH. While the nitrogen chemistry is regulated by additional factors, it appears still related to the CH_3OH chemistry.

4. A warm-up model for low-mass protostars produces COM abundances in fair agreement with observations: the relative abundances of most molecules follow the same trend as seen observationally, though with a systematic underestimation due to an excess of CH_3OH in the model. Most molecules are produced in the model by cold to lukewarm chemistry, consistent with observed rotational temperatures. CH_3CHO is an exception, occurring at much higher temperatures in the model compared to observations. Gas-phase chemistry is responsible for lukewarm CH_3CN production in the model, driven by high HCN abundances.

5. LYSO COM abundances are comparable to measurements in solar system comets, indicating that the sun is fairly typical among low-mass stars.

The study is based on observations with the IRAM 30m Telescope. IRAM is supported by INSU/CNRS (France), MPG (Germany) and IGN (Spain). J.B.B acknowledges funding from the National Science Foundation Graduate Research Fellowship under Grant DGE1144152. K.I.O. acknowledges funding from the Simons Collaboration on the Origins of Life (SCOL) investigator award.

7. APPENDIX: DETECTION SPECTRA

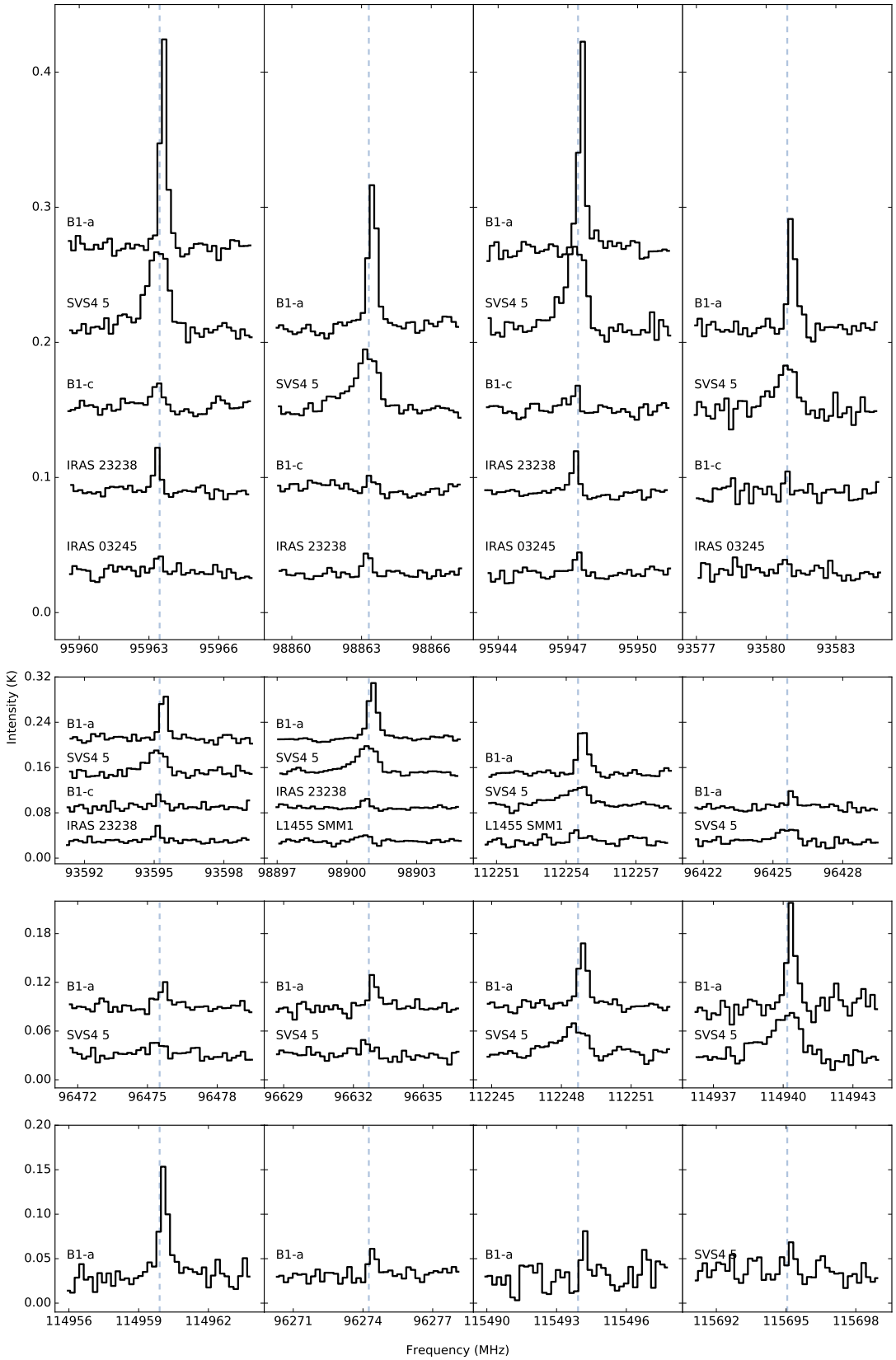

Figure 15. CH_3CHO detected transitions. Grey dashed lines show line centers; spectra are offset for clarity.

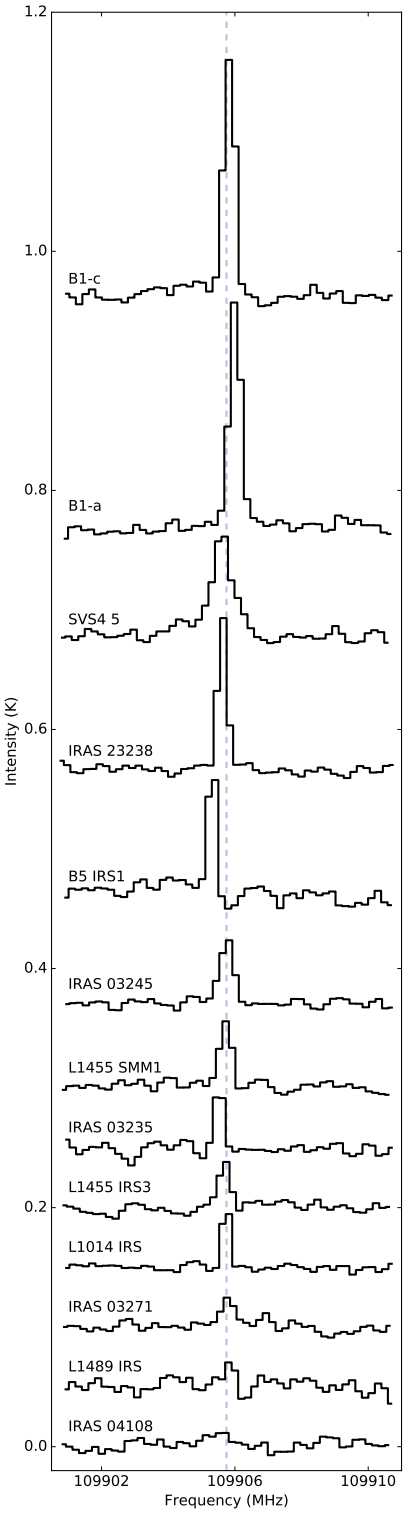

Figure 16. HNCO detected transitions. Grey dashed lines show line centers; spectra are offset for clarity.

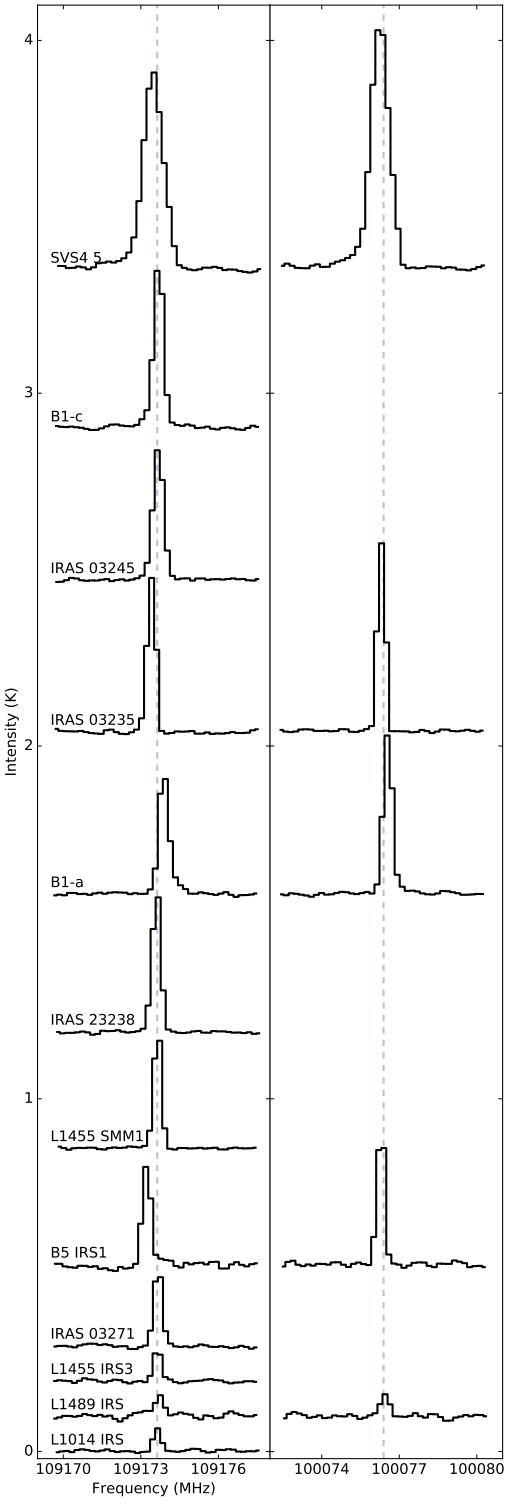

Figure 17. HC_3N detected transitions. Grey dashed lines show line centers; spectra are offset for clarity.

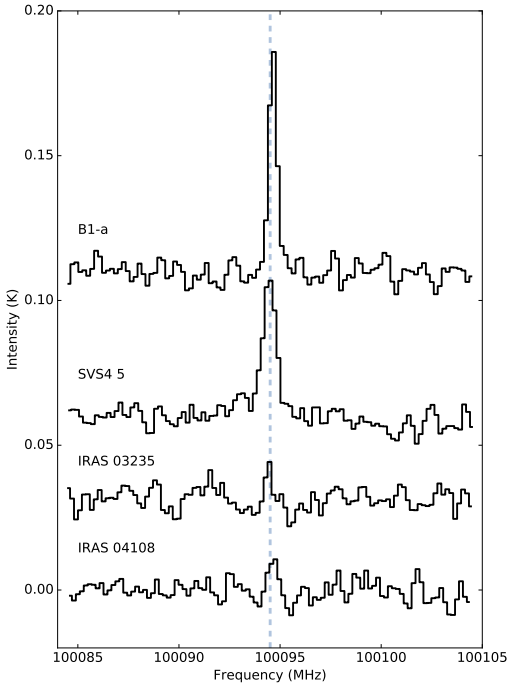

Figure 18. CH_2CO detected transitions. Grey dashed lines show line centers; spectra are offset for clarity.

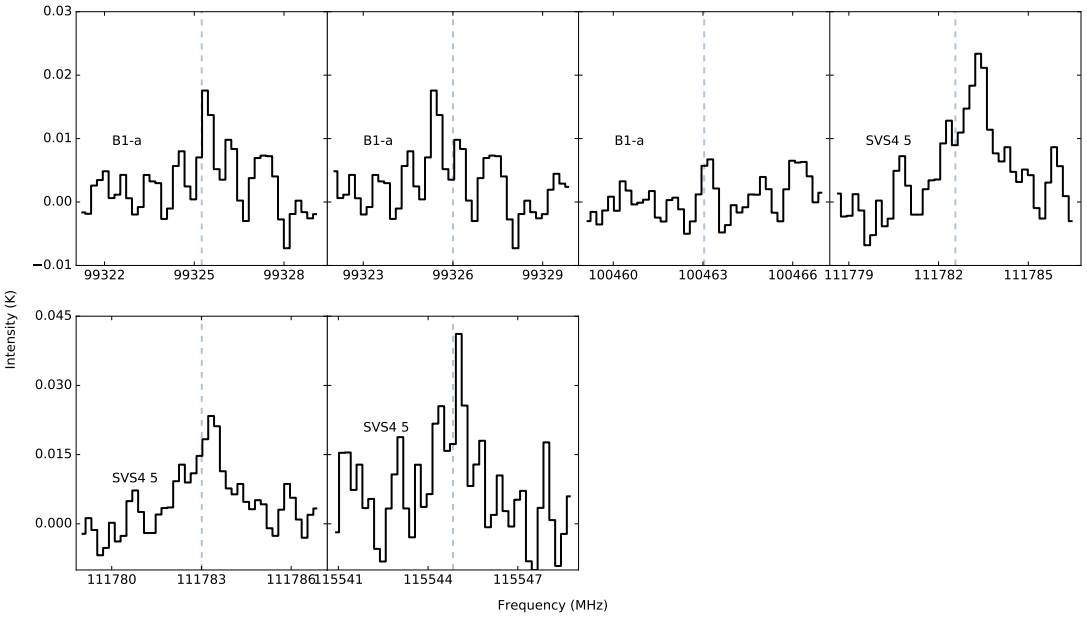

Figure 19. CH_3OCH_3 detected transitions. Grey dashed lines show line centers; spectra are offset for clarity.

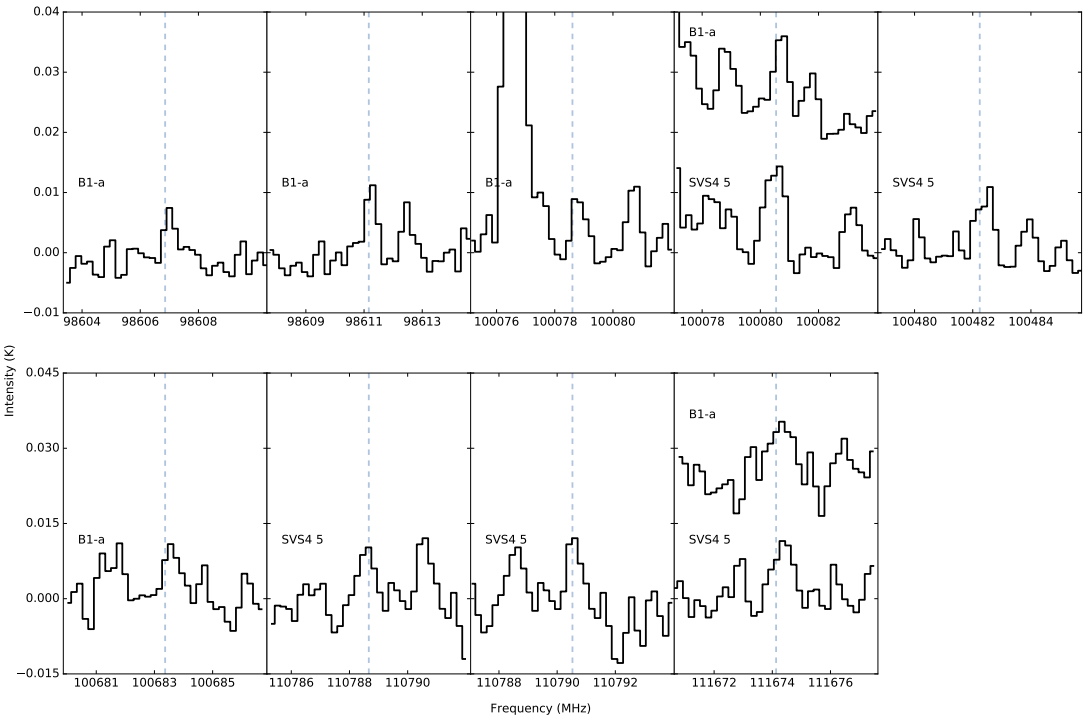

Figure 20. CH_3OCHO detected transitions. Grey dashed lines show line centers; spectra are offset for clarity.

8. APPENDIX: ROTATION DIAGRAMS

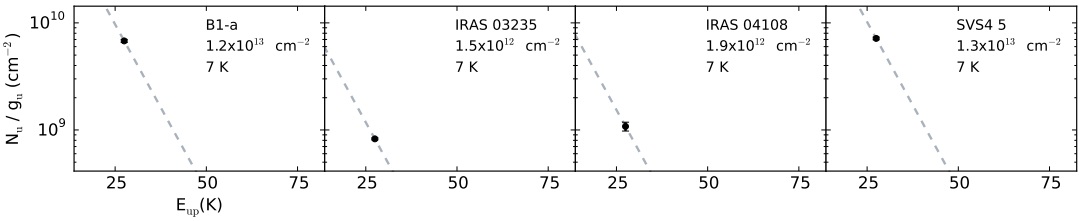

Figure 21. Rotation diagrams for CH_2CO. Black circles indicate detections and grey triangles indicate upper limits. Black dashed lines represent the fits to the data. When a line could not be fit, a rotational temperature was assumed as described in the text, shown in grey dashed lines.

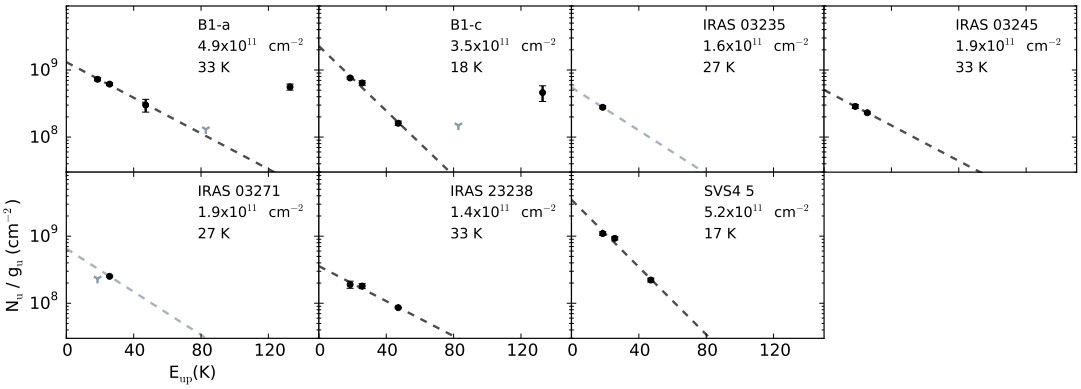

Figure 22. Rotation diagrams for CH_3CN. Black circles indicate detections and grey triangles indicate upper limits. Black dashed lines represent the fits to the data. When a line could not be fit, a rotational temperature was assumed as described in the text, shown in grey dashed lines.

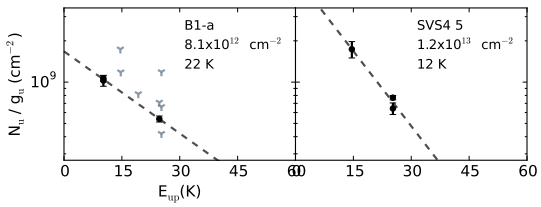

Figure 23. Rotation diagram for CH_3OCH_3. Black circles indicate detections and grey triangles indicate upper limits. Black dashed lines represent the fits to the data. When a line could not be fit, a rotational temperature was assumed as described in the text, shown in grey dashed lines.

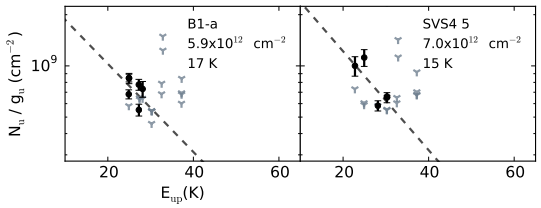

Figure 24. Rotation diagrams for CH_3OCHO. Black circles indicate detections and grey triangles indicate upper limits. Black dashed lines represent the fits to the data. When a line could not be fit, a rotational temperature was assumed as described in the text, shown in grey dashed lines.

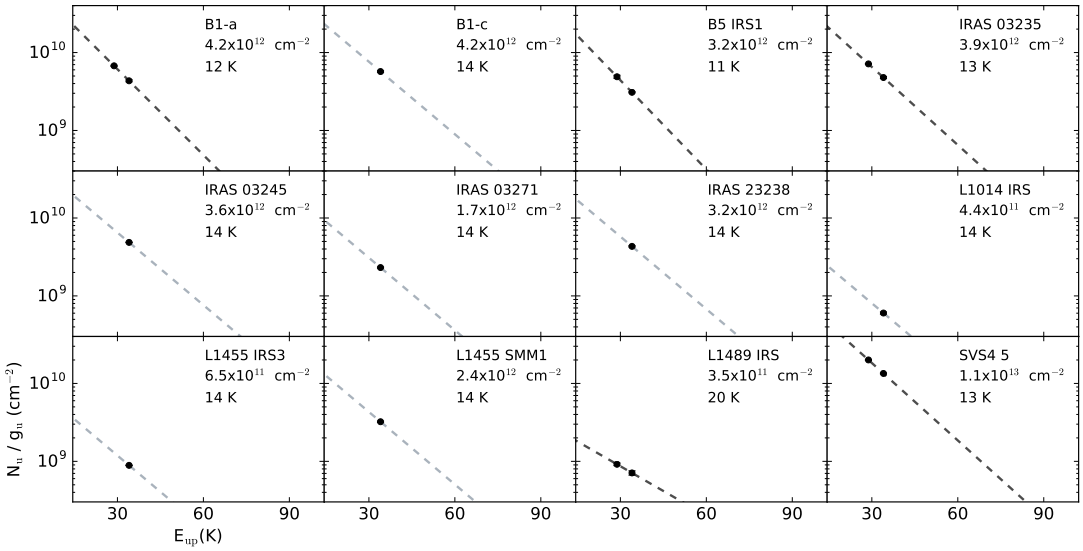

Figure 25. Rotation diagrams for HC_3N. Black circles indicate detections and grey triangles indicate upper limits. Black dashed lines represent the fits to the data. When a line could not be fit, a rotational temperature was assumed as described in the text, shown in grey dashed lines.

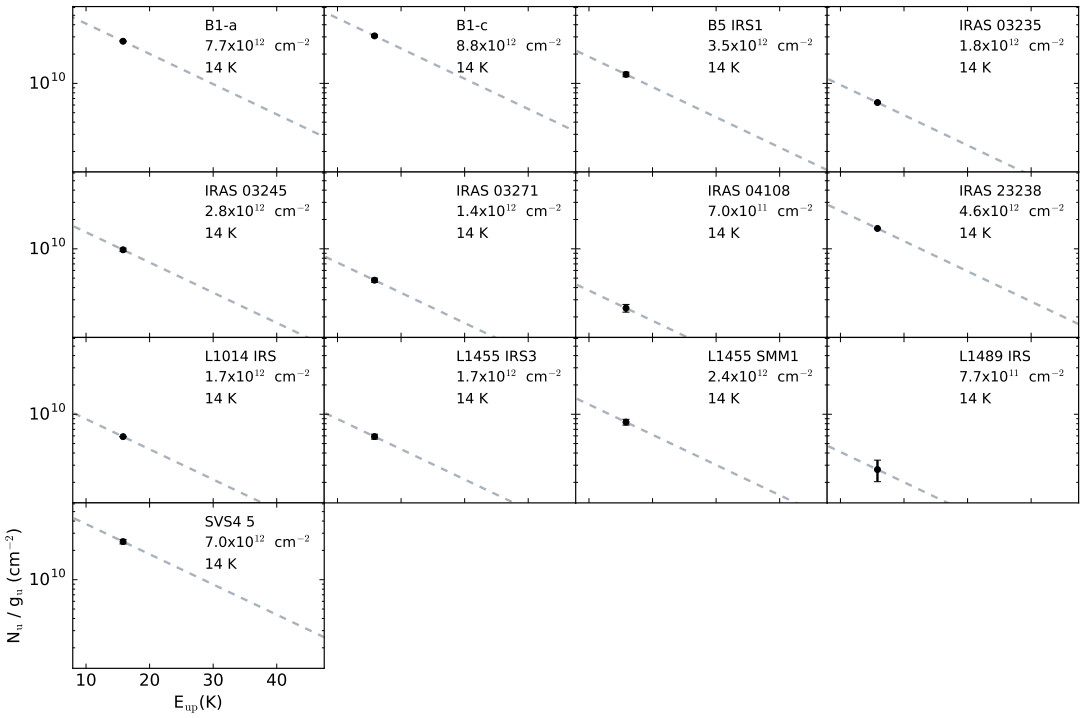

Figure 26. Rotation diagrams for HNCO. Black circles indicate detections and grey triangles indicate upper limits. Black dashed lines represent the fits to the data. When a line could not be fit, a rotational temperature was assumed as described in the text, shown in grey dashed lines.

9. APPENDIX: OBSERVED TRANSITIONS AND UPPER LIMITS

Table 6. Observed CH_2CO line intensities

Freq. (GHz)	Transition	$\int T_{MB} dV$ (K km s^{-1})					
		B1-a	SVS 4-5	B5 IRS1	IRAS 03235	IRAS 04108	L1489 IRS
100.095	$5_{1,5}$ - $4_{1,4}$	0.117 (0.004)	0.124 (0.004)	<0.006	0.014 (0.000)	0.019 (0.002)	<0.006

Table 7. Observed CH_3CHO line intensities

Freq. (GHz)	Transition	$\int T_{MB} dV$ (K km s^{-1})							
		B1-a	SVS 4-5	B1-c	B5 IRS1	HH 300	IRAS 03235	IRAS 03245	IRAS 03254
93.581	$5_{1,5}$ - $4_{1,4}$ A	0.104 (0.009)	0.107 (0.006)	-	-	-	-	-	-
93.595	$5_{1,5}$ - $4_{1,4}$ E	0.099 (0.004)	0.124 (0.009)	0.023 (0.001)	-	-	-	-	-
95.947	$5_{0,5}$ - $4_{0,4}$ E	0.159 (0.007)	0.190 (0.010)	-	-	-	-	0.018 (0.004)	-
95.963	$5_{0,5}$ - $4_{0,4}$ A	0.172 (0.005)	0.197 (0.011)	0.033 (0.001)	<0.010	<0.004	<0.006	-	<0.006
96.274	$5_{2,4}$ - $4_{2,3}$ A	0.036 (0.007)	<0.011	-	-	-	-	-	-
96.426	$5_{2,4}$ - $4_{2,3}$ E	0.034 (0.006)	0.073 (0.007)	-	-	-	-	-	-
96.476	$5_{2,3}$ - $4_{2,2}$ E	0.040 (0.005)	0.036 (0.006)	-	-	-	-	-	-
96.633	$5_{2,3}$ - $4_{2,2}$ A	0.053 (0.011)	0.035 (0.000)	-	-	-	-	-	-
98.863	$5_{1,4}$ - $4_{1,3}$ E	0.148 (0.004)	0.146 (0.007)	0.013 (0.003)	-	-	-	<0.004	-
98.901	$5_{1,4}$ - $4_{1,3}$ A	0.144 (0.006)	0.159 (0.009)	<0.006	-	-	-	<0.003	-
112.249	$6_{1,6}$ - $5_{1,5}$ A	0.098 (0.005)	0.108 (0.009)	<0.011	-	-	-	<0.007	-
112.255	$6_{1,6}$ - $5_{1,5}$ E	0.110 (0.005)	0.104 (0.008)	<0.011	-	-	-	<0.008	-
114.940	$6_{0,6}$ - $5_{0,5}$ E	0.135 (0.011)	0.204 (0.011)	<0.022	-	-	-	<0.009	-
114.960	$6_{0,6}$ - $5_{0,5}$ A	0.135 (0.010)	0.143 (0.013)	<0.018	-	-	-	-	-
115.494	$6_{2,5}$ - $5_{2,4}$ A	0.038 (0.009)	<0.023	-	-	-	-	-	-
115.695	$6_{2,5}$ - $5_{2,4}$ E	0.071 (0.005)	<0.020	-	-	-	-	-	-
115.910	$6_{2,4}$ - $5_{2,3}$ E	<0.018	<0.022	-	-	-	-	-	-
116.118	$6_{2,4}$ - $5_{2,3}$ A	<0.021	0.059 (0.004)	-	-	-	-	-	-
		IRAS 03271	IRAS 04108	IRAS 23238	L1014 IRS	L1448 IRS1	L1455 IRS3	L1455 SMM1	L1489 IRS
93.581	$5_{1,5}$ - $4_{1,4}$ A	-	-	-	-	-	-	-	-
93.595	$5_{1,5}$ - $4_{1,4}$ E	-	-	0.025 (0.000)	-	-	-	-	-
95.947	$5_{0,5}$ - $4_{0,4}$ E	-	-	0.035 (0.004)	-	-	-	-	-
95.963	$5_{0,5}$ - $4_{0,4}$ A	<0.004	<0.007	0.032 (0.002)	<0.003	<0.004	<0.004	-	<0.008
98.863	$5_{1,4}$ - $4_{1,3}$ E	-	-	0.021 (0.001)	-	-	-	-	-
98.901	$5_{1,4}$ - $4_{1,3}$ A	-	-	0.020 (0.000)	-	-	-	0.025 (0.004)	-
112.249	$6_{1,6}$ - $5_{1,5}$ A	-	-	<0.006	-	-	-	<0.008	-
112.255	$6_{1,6}$ - $5_{1,5}$ E	-	-	<0.005	-	-	-	0.022 (0.000)	-
114.940	$6_{0,6}$ - $5_{0,5}$ E	-	-	<0.008	-	-	-	<0.013	-
114.960	$6_{0,6}$ - $5_{0,5}$ A	-	-	<0.009	-	-	-	<0.013	-
115.494	$6_{2,5}$ - $5_{2,4}$ A	-	-	-	-	-	-	<0.015	-

Table 8. Observed CH_3CN line intensities

Freq. (GHz)	Transition	$\int T_{MB} dV$ (K km s^{-1})							
		B1-a	SVS 4-5	B1-c	B5 IRS1	HH 300	IRAS 03235	IRAS 03245	IRAS 03254
110.349	6_4 - 5_4 110.349	6(4) - 5(4)	0.026 (0.003)	-	0.022 (0.006)	-	-	-	-
110.364	6_3 - 5_3 110.364	6(2) - 5(2)	<0.005	-	<0.006	-	-	-	-
110.375	6_2 - 5_2 110.375	6(1) - 5(1)	0.022 (0.005)	0.017 (0.001)	0.012 (0.001)	-	-	-	-
110.381	6_1 - 5_1 110.381	6(0) - 5(0)	0.050 (0.002)	0.076 (0.004)	0.052 (0.004)	-	-	-	0.019 (0.001)
110.383	6_0 - 5_0 110.383	6(4) - 5(4)	0.061 (0.003)	0.092 (0.006)	0.064 (0.003)	<0.008	<0.006	0.023 (0.001)	0.024 (0.002)
		IRAS 03271	IRAS 04108	IRAS 23238	L1014 IRS	L1448 IRS1	L1455 IRS3	L1455 SMM1	L1489 IRS
110.375	6_2 - 5_2	-	-	0.006 (0.000)	-	-	-	-	-
110.381	6_1 - 5_1	0.021 (0.000)	-	0.015 (0.001)	-	-	-	-	-
110.383	6_0 - 5_0	<0.007	<0.006	0.016 (0.002)	<0.003	<0.005	<0.004	<0.005	<0.007

Table 9. Observed CH_3OCH_3 line intensities

Freq. (GHz)	Transition	$\int T_{MB} dV$ (K km s^{-1})							
		B1-a	SVS 4-5	B1-c	B5 IRS1	HH 300	IRAS 03235	IRAS 03245	IRAS 03254
93.857	$4_{2,3}$ - $4_{1,4}$ EE	<0.005	-	-	-	-	-	-	-
96.850	$5_{2,4}$ - $5_{1,5}$ EE	<0.004	-	-	-	-	-	-	-
99.325	$4_{1,4}$ - $3_{0,3}$ EE	0.017 (0.001)	-	-	-	-	-	-	-
99.326	$4_{1,4}$ - $3_{0,3}$ AA	0.011 (0.001)	-	<0.006	<0.006	<0.004	<0.004	<0.003	<0.005
100.463	$6_{2,5}$ - $6_{1,6}$ EE	0.010 (0.000)	-	-	-	-	-	-	-
100.466	$6_{2,5}$ - $6_{1,6}$ AA	<0.003	-	-	-	-	-	-	-
111.783	$7_{0,7}$ - $6_{1,6}$ AA	<0.004	0.012 (0.001)	-	-	-	-	-	-
111.783	$7_{0,7}$ - $6_{1,6}$ EE	<0.004	0.022 (0.001)	-	-	-	-	-	-
111.784	$7_{0,7}$ - $7_{1,6}$ AE	<0.004	-	-	-	-	-	-	-
115.545	$5_{1,5}$ - $4_{0,4}$ EE	<0.014	0.041 (0.006)	-	-	-	-	-	-
		IRAS 03271	IRAS 04108	IRAS 23238	L1014 IRS	L1448 IRS1	L1455 IRS3	L1455 SMM1	L1489 IRS
99.326	$4_{1,4}$ - $3_{0,3}$ AA	<0.005	<0.004	<0.003	<0.002	<0.003	<0.005	<0.004	<0.005

Table 10. Observed CH_3OCHO line intensities

Freq. (GHz)	Transition	$\int T_{MB} dV$ (K km s^{-1})							
		B1-a	SVS 4-5	B1-c	B5 IRS1	HH 300	IRAS 03235	IRAS 03245	IRAS 03254
98.607	$8_{3,6}$ - $7_{3,5}$ E	0.012 (0.001)	-	-	-	-	-	-	-
98.611	$8_{3,6}$ - $7_{3,5}$ A	0.017 (0.001)	-	<0.008	<0.007	<0.005	<0.003	<0.005	<0.004
100.079	$9_{1,9}$ - $8_{1,8}$ E	0.024 (0.002)	<0.007	-	-	-	-	-	-
100.081	$9_{1,9}$ - $8_{1,8}$ A	0.024 (0.001)	0.032 (0.004)	-	-	-	-	-	-
100.295	$8_{3,5}$ - $7_{3,4}$ E	<0.005	-	-	-	-	-	-	-
100.308	$8_{3,5}$ - $7_{3,4}$ A	<0.005	-	-	-	-	-	-	-

Table 10 continued

Table 10 *(continued)*

Freq. (GHz)	Transition	$\int T_{MB} dV$ (K km s^{-1})							
100.482	$8_{1,7}$ - $7_{1,6}$ E	-	0.025 (0.003)	-	-	-	-	-	-
100.491	$8_{1,7}$ - $7_{1,6}$ A	-	<0.006	-	-	-	-	-	-
100.682	$9_{0,9}$ - $8_{0,8}$ E	<0.006	<0.006	-	-	-	-	-	-
100.683	$9_{0,9}$ - $8_{0,8}$ A	0.019 (0.001)	<0.006	-	-	-	-	-	-
110.789	$10_{1,10}$ - $9_{1,9}$ E	<0.006	0.023 (0.000)	-	-	-	-	-	-
110.791	$10_{1,10}$ - $9_{1,9}$ A	<0.006	0.023 (0.002)	-	-	-	-	-	-
110.880	$9_{5,5}$ - $8_{5,4}$ A	<0.007	<0.006	-	-	-	-	-	-
110.887	$9_{3,7}$ - $8_{3,6}$ A	<0.006	<0.006	-	-	-	-	-	-
111.170	$10_{0,10}$ - $9_{0,9}$ E	<0.006	<0.006	-	-	-	-	-	-
111.172	$10_{0,10}$ - $9_{0,9}$ A	<0.005	<0.006	-	-	-	-	-	-
111.196	$9_{4,6}$ - $8_{4,5}$ A	<0.005	<0.006	-	-	-	-	-	-
111.223	$9_{4,6}$ - $8_{4,5}$ E	<0.006	<0.007	-	-	-	-	-	-
111.408	$9_{4,5}$ - $8_{4,4}$ E	<0.007	<0.005	-	-	-	-	-	-
111.453	$9_{4,5}$ - $8_{4,4}$ A	<0.006	<0.006	-	-	-	-	-	-
111.674	$9_{1,8}$ - $8_{1,7}$ E	0.023 (0.002)	0.018 (0.001)	-	-	-	-	-	-
111.682	$9_{1,8}$ - $8_{1,7}$ A	<0.007	<0.006	-	-	-	-	-	-
113.743	$9_{3,6}$ - $8_{3,5}$ E	<0.012	<0.011	-	-	-	-	-	-
113.757	$9_{3,6}$ - $8_{3,5}$ A	<0.014	<0.014	-	-	-	-	-	-
116.545	$9_{2,7}$ - $8_{2,6}$ E	<0.029	<0.025	-	-	-	-	-	-
116.558	$9_{2,7}$ - $8_{2,6}$ A	<0.033	<0.027	-	-	-	-	-	-
		IRAS 03271	IRAS 04108	IRAS 23238	L1014 IRS	L1448 IRS1	L1455 IRS3	L1455 SMM1	L1489 IRS
98.611	$8_{3,6}$ - $7_{3,5}$ A	<0.004	<0.005	<0.003	<0.003	<0.003	<0.004	<0.004	<0.005

Table 11. Observed HC_3N line intensities

Freq. (GHz)	Transition	$\int T_{MB} dV$ (K km s^{-1})							
		B1-a	SVS 4-5	B1-c	B5 IRS1	HH 300	IRAS 03235	IRAS 03245	IRAS 03254
100.076	11-10	0.620 (0.010)	1.839 (0.029)	-	0.449 (0.020)	-	0.657 (0.007)	-	-
109.174	12-11	0.474 (0.014)	1.467 (0.019)	0.624 (0.014)	0.337 (0.006)	<0.007	0.522 (0.015)	0.531 (0.004)	<0.005
		IRAS 03271	IRAS 04108	IRAS 23238	L1014 IRS	L1448 IRS1	L1455 IRS3	L1455 SMM1	L1489 IRS
100.076	11-10	-	-	-	-	-	-	-	0.084 (0.003)
109.174	12-11	0.253 (0.004)	<0.005	0.472 (0.009)	0.066 (0.002)	<0.004	0.097 (0.001)	0.352 (0.007)	0.078 (0.005)

Table 12. Observed HNCO line intensities

Freq. (GHz)	Transition	$\int T_{MB} dV$ (K km s^{-1})							
		B1-a	SVS 4-5	B1-c	B5 IRS1	HH 300	IRAS 03235	IRAS 03245	IRAS 03254
109.906	$5_{0,5}$ - $4_{0,4}$	0.228 (0.002)	0.191 (0.010)	0.247 (0.007)	0.097 (0.005)	<0.006	0.050 (0.001)	0.076 (0.003)	<0.006
		IRAS 03271	IRAS 04108	IRAS 23238	L1014 IRS	L1448 IRS1	L1455 IRS3	L1455 SMM1	L1489 IRS

Table 12 continued

Table 12 *(continued)*

Freq. (GHz)	Transition	$\int T_{MB} dV$ (K km s^{-1})							
109.906	$5_{0,5}$ - $4_{0,4}$	0.037 (0.002)	0.019 (0.002)	0.126 (0.000)	0.046 (0.000)	<0.004	0.046 (0.003)	0.064 (0.004)	0.021 (0.005)

REFERENCES

Arce, H. G., Santiago-García, J., Jørgensen, J. K., Tafalla, M., & Bachiller, R. 2008, ApJL, 681, L21

Bacmann, A., Taquet, V., Faure, A., Kahane, C., & Ceccarelli, C. 2012, A&A, 541, L12

Balucani, N., Ceccarelli, C., & Taquet, V. 2015, MNRAS, 449, L16

Belloche, A., Meshcheryakov, A. A., Garrod, R. T., et al. 2017, arXiv:1701.04640, A&Ain press

Bennett, C. J., Jamieson, C. S., Osamura, Y., & Kaiser, R. I. 2005, ApJ, 624, 1097

Bisschop, S. E., Jørgensen, J. K., Bourke, T. L., Bottinelli, S., & van Dishoeck, E. F. 2008, A&A, 488, 959

Bisschop, S. E., Jørgensen, J. K., van Dishoeck, E. F., & de Wachter, E. B. M. 2007, A&A, 465, 913

Blake, G. A., Sutton, E. C., Masson, C. R., & Phillips, T. G. 1987, ApJ, 315, 621

Boogert, A. C. A., Pontoppidan, K. M., Knez, C., et al. 2008, ApJ, 678, 985

Bottinelli, S., Ceccarelli, C., Williams, J. P., & Lefloch, B. 2007, A&A, 463, 601

Bottinelli, S., Ceccarelli, C., Lefloch, B., et al. 2004a, ApJ, 615, 354

Bottinelli, S., Ceccarelli, C., Neri, R., et al. 2004b, ApJL, 617, L69

Bottinelli, S., Boogert, A. C. A., Bouwman, J., et al. 2010, ApJ, 718, 1100

Brinch, C., Crapsi, A., Jørgensen, J. K., Hogerheijde, M. R., & Hill, T. 2007, A&A, 475, 915

Caselli, P., & Ceccarelli, C. 2012, A&A Rv, 20, 56

Cazaux, S., Tielens, A. G. G. M., Ceccarelli, C., et al. 2003, ApJL, 593, L51

Cernicharo, J., Marcelino, N., Roueff, E., et al. 2012, ApJL, 759, L43

Chandler, C. J., & Richer, J. S. 2000, ApJ, 530, 851

Crovisier, J., Bockelée-Morvan, D., Colom, P., et al. 2004, A&A, 418, 1141

Enoch, M. L., Corder, S., Dunham, M. M., & Duchêne, G. 2009, ApJ, 707, 103

Fayolle, E. C., Öberg, K. I., Garrod, R. T., van Dishoeck, E. F., & Bisschop, S. E. 2015, A&A, 576, A45

Fedoseev, G., Chuang, K.-J., van Dishoeck, E. F., Ioppolo, S., & Linnartz, H. 2016, MNRAS, 460, 4297

Fedoseev, G., Ioppolo, S., Zhao, D., Lamberts, T., & Linnartz, H. 2015, MNRAS, 446, 439

Feigelson, E. D., & Nelson, P. I. 1985, ApJ, 293, 192

Furlan, E., McClure, M., Calvet, N., et al. 2008, ApJS, 176, 184

Garrod, R. T. 2013, ApJ, 765, 60

Garrod, R. T., Belloche, A., Mueller, H. S. P., & Menten, K. M. 2017, arXiv:1701.07160, A&Ain press

Garrod, R. T., & Herbst, E. 2006, A&A, 457, 927

Garrod, R. T., Wakelam, V., & Herbst, E. 2007, A&A, 467, 1103

Garrod, R. T., Widicus Weaver, S. L., & Herbst, E. 2008, ApJ, 682, 283

Goesmann, F., Rosenbauer, H., Bredehöft, J. H., et al. 2015, Science, 349, doi:10.1126/science.aab0689

Goldsmith, P. F., & Langer, W. D. 1999, ApJ, 517, 209

Graninger, D. M., Wilkins, O. H., & Öberg, K. I. 2016, ApJ, 819, 140

Hatchell, J., Fuller, G. A., Richer, J. S., Harries, T. J., & Ladd, E. F. 2007, A&A, 468, 1009

Herbst, E., & van Dishoeck, E. F. 2009, ARA&A, 47, 427

Hudson, R. L., & Loeffler, M. J. 2013, ApJ, 773, 109

Jørgensen, J. K., Schöier, F. L., & van Dishoeck, E. F. 2002, A&A, 389, 908

Maity, S., Kaiser, R. I., & Jones, B. M. 2014, ApJ, 789, 36

Miller, R., Gong, G., & Muñoz, A. 1981, Survival Analysis, A Wiley-Interscience publication (Wiley)

Mumma, M. J., & Charnley, S. B. 2011, ARA&A, 49, 471

Öberg, K. I. 2016, ChRv, 116(17), 9631

Öberg, K. I., Boamah, M. D., Fayolle, E. C., et al. 2013, ApJ, 771, 95

Öberg, K. I., Boogert, A. C. A., Pontoppidan, K. M., et al. 2011a, ApJ, 740, 109

Öberg, K. I., Bottinelli, S., Jørgensen, J. K., & van Dishoeck, E. F. 2010, ApJ, 716, 825

Öberg, K. I., Garrod, R. T., van Dishoeck, E. F., & Linnartz, H. 2009, A&A, 504, 891

Öberg, K. I., Lauck, T., & Graninger, D. 2014, ApJ, 788, 68

Öberg, K. I., van der Marel, N., Kristensen, L. E., & van Dishoeck, E. F. 2011b, ApJ, 740, 14

Pontoppidan, K. M., van Dishoeck, E. F., & Dartois, E. 2004, A&A, 426, 925

Schöier, F. L., van der Tak, F. F. S., van Dishoeck, E. F., & Black, J. H. 2005, A&A, 432, 369

van der Tak, F. F. S., Black, J. H., Schöier, F. L., Jansen, D. J. & van Dishoeck, E. F. 2007, A&A, 468, 627

van Dishoeck, E. F., Blake, G. A., Jansen, D. J., & Groesbeck, T. D. 1995, ApJ, 447, 760

Visser, R., Doty, S. D., & van Dishoeck, E. F. 2011, A&A, 534, A132

Visser, R., van Dishoeck, E. F., Doty, S. D., & Dullemond, C. P. 2009, A&A, 495, 881